Modal and Impact Analysis of Fluid-Structure Interaction by Finite Element Methods.

by

Akshay Mallikarjuna

A dissertation submitted to the Graduate Faculty of
Auburn University
in partial fulfillment of the
requirements for the Degree of
Doctor of Philosophy

Auburn, Alabama
December 11, 2021

Keywords: FEM, Modal Analysis, Coupling Factor, Impact, Fluid-Structure Interaction

Approved by

P.K.Raju, Chair, Thomas Walter Distinguished Professor Emeritus of Mechanical Engineering
Dan Marghitu, Co-Chair, Professor of Mechanical Engineering
Andrzej S. Nowak, Professor, Elton and Lois G. Huff Eminent Scholar and Department Chair of Civil Engineering
Edmon Perkins, Assistant Professor of Mechanical and Aerospace Engineering, North Carolina State University
N K Govil, Professor Emeritus of Mathematics and Statistics

Abstract

In this work, the modal and impact interactions of fluid-filled cylindrical structures are studied. The first part of the study focuses on the parametric modal analysis of fluid-coupled thin structures. This study emphasizes describing or approximating the coupled natural frequency of a fluid filled structure as a function of respective modes of the uncoupled structures. A condition to differentiate the strong and weak coupling between fluid and structure is proposed. In the second part of the study, an optimized method to simulate the dynamic 3D event of the impact of a rod with a flat surface is presented. Unlike in the 2D FEM (Finite Element Method) based contact models, in this study, both bodies undergoing the impact are considered elastic-plastic(deformable) and simulation is the dynamic event of the impact, instead of predefined 2D symmetric contact analysis. Prominent contact models and plasticity models to define material properties in ANSYS are reviewed. The coefficient of restitution (COR) for normal and oblique impact of the rods are obtained by experimentation. Experimental results of the permanent deformation on the base for different impact velocities is derived from a prominent impact study. The simulation results are in co-relation with the experiment and both indentation and flattening models on the COR and permanent deformation of the base and rod after the impact. Thus, the presented 3D explicit dynamic simulation of impact is validated to analyze the impact behavior of the two bodies without any predefined assumptions with respect to boundary conditions or material properties. Furthermore, this validated finite element method is used to simulate the impact of fluid-filled tubes. The effect of coupling on contact parameters (deformation, COR, contact force, and plastic work) is analyzed for the normal impact. It is observed that during the impact of the inclined rods and tubes, there are multiple impacts during the event. Finally, it is shown that the natural frequency of the impacting rod has a significant

effect on this behavior. For the future studies, analytical modeling of the impact should also consider the vibration and natural frequency of the system in the equation of motion.

Acknowledgments

I would like to thank everyone who assisted me throughout my doctoral studies over the years. First, I would like to thank Dr.P.K.Raju, my advisor, for believing in me, for giving me the priceless opportunity to pursue a PhD, and for his guidance and encouragement. I would alo like to acknowledge my co-advisor, Dr.Dan Marghitu, for his valuable guidance, through which I was able to pursue and complete my research at Auburn University. Special thanks to Dr.Dejang Shang, a visiting professor from Harbin Engineering University, for playing a significant role in mentoring me in this new area of research. I would like to thank Ms.Jing Zaho, who helped me through the experiments. I also thank Dr.Jeff Suhling, the Department Chair of Mechanical Engineering, for his valuable support. I would like to acknowledge the support of all my friends that I made in Auburn who always cared for me. Special thanks to my younger brother, Dr.Ashwin Mallikarjuna for his support and encouragement in this remarkable journey. I also thank my committee members, Dr.Andrzej S.Nowak, Dr.Edmon Perkins, and Dr.N K Govil, for all their support and guidance through this process.
Finally, I would like to dedicate this dissertation and all of my success to my parents, Ms.Uma Mallikarjuna and Mr.Mallikarjuna Sadashivappa. I am blessed and grateful for their constant support, love, and sacrifice as being the main reasons for my success with this dissertation and other accomplishments in my life.

Table of Contents

List of Figures

List of Tables

Chapter 1

Introduction

The finite element method (FEM) is a numerical method used to solve a mathematical model of a given complex structure or system, for which analytical closed-form solutions are generally not possible. FEM analysis can be used to help evaluate the feasibility of a design without having to build a physical prototype for the complex systems, since we can specify the actual shape, load, constraints, and material property combinations with great accuracy. Finite element analysis (FEA) also allows engineers to interpret results in very sophisticated ways using vector plots and graphical interface to visualize, read, and analyze the result, but it is important to understand that FEM only gives an approximate solution to the problem and is a numerical approach to getting the real results of the variational formulation of partial differential equations. A finite element based numerical approach lends itself to a number of assumptions and uncertainties related to domain discretizations, mathematical shape functions, solution procedures, etc. This fully-virtual product development and analysis methodology leads to a situation wherein a misinterpreted approximation or error in applying a load condition may be carried throughout the engineering lifecycle, leading to a situation where the errors get cumulative at each stage, producing disastrous results. FEM analysis is only as good as the structure of the simulation. FEA involves four steps: model development, verification, predictive calculations, and uncertainty assessment and finally validation of results alongside the experiment or proven theory. To make sure you get accurate results using FEA, it is important to establish engineering criteria for use in the design evaluation. Determining where to use symmetry, how much of the structure needs to be modeled, type of analysis and accounting for non-linearity are a few of the many criteria which require engineering judgement to proceed further to setup the simulation. In setting

up a FEM model for the simulation, it should be ensured that the boundary conditions and loading match the experimental setup. Determining the mesh distribution, mesh density, and locations in the model where the mesh density is critical are equally important in finite element simulation, hence, verification and validation are required in FEA projects to provide confidence that the computational model developed performs within the required parameters. The verification procedure includes checking the design and investigating whether the computational model accurately represents the physical system. Validation is more of a dynamic procedure and determines if the computational simulation agrees with the physical phenomenon; it examines the difference between the numerical simulation and the experimental results. Verification provides information about whether the computational model is solved correctly and accurately, while validation provides evidence regarding the extent to which the mathematical model accurately correlates to the theory and experiment. In our study, all the necessary steps are taken in validating the FEM analysis.

1.1 Theory and historical background on structures vibrating under the influence of fluid

Cylindrical shells are often used as vessels for storing and transporting liquid. Obviously, the existence of a fluid medium will have an important effect on the dynamic response behavior of cylindrical shells. A structure vibrating in contact with the fluid of a comparable density experiences loading that is proportional to the fluid's inertial and elastic forces. Fluid loading thus modifies the forces acting on the structure and, since these acoustic pressures depend on the velocity, a feedback coupling between the fluid and the structure exists. Hence, the structural and acoustical domains must be accounted for simultaneously. The two domains are said to be coupled when boundary conditions ensure the continuity in displacement and pressure normal to the surface of the structure and fluid at the interface. Studies on vibroacoustics (structural acoustics) on pipes and cylinders date back to the late 19th and early 20th centuries with the work of Rayleigh, Lamb, Love, and Stokes

with mathematical descriptions. Beginning in 1966, Ram Kumar and others[33] analyzed cylinder vibration and wave propagation in fluid-filled cylinders using the exact linear elastic theory, and both axisymmetric and symmetric vibration involving bending and flexural modes are discussed in this paper. The main emphasis of this paper is calculation of the propagation speeds for each mode as a function of frequency. In 1972, Miguel C. Junger[27] in the book *Sound Structure and Their Interactions* discussed intensively the integrated equation of structure-fluid interaction and also formulated the equations for normal modes of general structures coupled with fluids. The discussion here is restricted to specific boundary conditions and modes of vibration.

Fluid-structure interaction is formulated at different levels of physical representation complexity. From the classical Westergaard, or $added - mass$, approach, fluid incomprehensibility and rigid structure are assumed to the modern fluid-structure coupled boundary interface approach using finite element analysis software. It is necessary to study the fluid-structure interaction problems in a coupled manner considering the flexibility effect of the structure and the compressibility of the fluid. Formulations based on displacement variables are generally chosen for the structure, while the fluid is described by different variables, such as displacement, pressure, velocity potential, etc., for such coupled problems. The governing differential equation for the displacement at the structural interface is formulated as the following:

The governing equation for the pressure field for the exterior and interior fluids is

$$\nabla^2 p - c_s^2 \frac{\delta^2 p}{\delta t^2} = 0 \tag{1.1}$$

where;

ρ = Density of the structural materials

u = Displacement vector of the cylinder wall

p = Pressure field of the fluid

λ, μ = Lame's constant (Material Properties)

c_s = Phase velocity of the structure-borne sound wave

∇ = Gradient of displacement

These equations are general for all coupled linear acoustoelastic problems; imposing particular boundary conditions makes them specific. Typically, these are a continuity of normal stress (pressure) and normal displacement at the interface between fluid and solid, and zero shear stress since fluid viscosity is usually negligible. Analytic expressions for the solutions of these equations and boundary conditions are possible for specific systems, such as spheres and cylindrical pipes of infinite length, which are subjected to a specific boundary condition.

Prior to 1980, most of the analyses of vibrations from pipes regarded them as cylindrical shells of infinite length in isolation from other structures. Furthermore, in 1980's, the increased capabilities of computers permitted the analysis of more complicated vibration problems using the finite element method. Finite element formulation[50, 49, 51, 52, 53] of the governing equations, including the coupling conditions, ensures that the system of an equation of motion for an undamped structure-acoustic problem can be written in the form;

$$\begin{bmatrix} M_S & 0 \\ \rho_0 c^2 H_{SF}^T & M_F \end{bmatrix} \begin{bmatrix} \ddot{d}_S \\ \ddot{P}_F \end{bmatrix} + \begin{bmatrix} K_S & -H_{SF} \\ 0 & K_F \end{bmatrix} \begin{bmatrix} d_S \\ P_F \end{bmatrix} = \begin{bmatrix} f_b \\ f_q \end{bmatrix} \tag{1.2}$$

where;

d_S = Displacement variable in the structural domain

P_F = Nodal pressure

M_S, M_F = Mass matrix of the structure and fluid respectively

H_{SF} = Spatial coupling matrix

K_S, K_F = Stiffness matrix of the structure and fluid respectively

ρ_0 = The static density of the fluid

c = Speed of sound in fluid

The primary variables are the displacements in the structural domain and the acoustic pressure in the fluid domain. It is evident that the two domains are inter-related. In fluid-filled shells, the coupled modal structure can be understood as an interaction between the empty shell modes and the acoustic modes in the fluid. For long or thick cylinders at the lowest frequencies, the shell modes are simple combinations of the empty shell modes (torsion, bending, extensional) and the plane wave acoustic mode. The fluid mass has a greater effect on the cylinder's radial and bending mode, adding its inertia to the oscillations of the cross-section. On the other hand, for thin cylinders when the radius to thickness ratio is large enough, radial modes are more prominent than bending modes, which are normally observed at higher frequencies in long and thick cylinders. Perhaps the most important modes for pipe vibration are the flexural and bending modes. In these modes, the pipe radius varies with both the angular and axial position. The coupling factor of the natural frequency can be linked to the variation in the flexural wave speed (V_F) of the cylinder when it is coupled with fluid[27]. Different means of finite element formulation of coupled structure-acoustic problems have been studied, starting from a basic analysis by Ottosen and Petersson[44] to more complicated dynamic response studied by Bathe[9].

$$V_F \;=\; \omega/k \tag{1.3}$$

Our description of cylinder vibration ignores any effect of the external fluid to the pipe. In many applications, the effect is minor (as the outer fluid is air) and can be ignored except when the analysis is of underwater acoustics or of very high modes and frequencies.

1.1.1 Theory on coupled cylinders

Let's consider a simple elastic shell structure enclosing the fluid. The cylinder wall is assumed to be locally reacting and therefore characterized by a specific acoustic reactance, X_w.

For a cylinder of radius a the radial velocity $\dot{\omega}$ is related to the pressure through the equation,

$$\dot{\omega} = -i\frac{(\delta p/\delta r)}{\rho c k} \tag{1.4}$$

The boundary condition for the interface can be explicitly stated as,

$$\frac{p}{(\delta p/\delta r)} = \frac{x_W}{\rho c k} \tag{1.5}$$

where,

x_W = Specific acoustic reactance.

For air-filled cylinders, the wall can be approximated as rigid. For a water-filled cylinder, the elastic property of the cylinder is not negligible and has an effect on wave propagation. Neglecting the longitudinal pipe vibration, an axisymmetric sound pressure produces a uniform radial deflection ω, which results in a hoop strain, ϵ, and stress, σ.

$$\epsilon = \frac{\omega}{a} \tag{1.6}$$

$$\sigma = \epsilon\frac{E}{1-\nu} \tag{1.7}$$

Interaction solutions are usually more readily interpreted when the structural elastic constants are expressed in terms of concepts related to the wave propagation. Hence the term $phase - velocity$ in a structure is introduced. For a plate, the phase velocity is given by,

$$c_P = [E/(1-\nu^2)\rho_s]^{1/2} \tag{1.8}$$

Compressibility of the acoustic fluid and wall elasticity combined enhances the fractional volume change which yields to compliance and in turn, change in sound velocity in the fluid given as a correction factor.

$$\begin{aligned} B_W^{-1} &= (dV/V)/p \\ &= 2\omega/ap \\ &= 2a/\rho_s c_p^2 h \end{aligned}$$

where,

B =Bulk Modulus of the fluid = ρc^2

The sound velocity can now be corrected for wall elasticity by noting that the compressibility of the acoustic fluid and of the pipe wall combine so as to enhance the fractional volume change:

$$c_0 = [\rho(B_W^{-1}/B^{-1})]^{-1/2} \tag{1.9}$$

To put this as a comparison or a correction factor,

$$c_0/c = [1 + (B_W^{-1}/B^{-1})]^{-1/2} \tag{1.10}$$

Substituting the Bulk modulus of the fluid, this equation then becomes;

$$c_0/c = [(1 + 2a\rho c^2/h\rho_s c_p^2)]^{-1/2} \tag{1.11}$$

This equation is called the Korteweg-Lamb Correction.

In a similar approach, by taking the cylindrical modes into consideration, this paper defines a correction factor for predicting the natural frequency of the coupled system for the given uncoupled natural frequency of the cylinder of the same mode.

1.2 Theory and historical background on low-velocity impact by rods

The comparison of the experimental results and the finite element analysis (FEA) of a low velocity impact of spheres and rods have gained attention since the beginning of 21^{st} century. To date, the impact models which are formulated are based on implicit 2D contact models with the predefined contact conditions. Normally, the contact models consider either the flat or the hemispherical body under motion as rigid. The models considering the impacting body as rigid are called indentation models, whereas models considering the fixed flat surface under impact as rigid are called flattening models. There are very few models which consider both the impacting body and the surface undergoing the impact as elastic. The present study validates a 3D explicit dynamics FEM[62] model using these contact models and experimental results of the impact, so that this FEM model can be used to simulate and analyze more complicated 3D asymmetric systems through a dynamic simulation of impact.

Hertz Contact Theory is the basis through which it is possible to study the impact of a fully elastic object. He established a closed form solution for the impact of 2 elastic spheres based on which other theories are formulated. However, Hertz theory is limited to only the elastic phase of the impact; the plasticity involved during the event of impact is not addressed in Hertz theory. Later, the study on indentation to measure the hardness of the material provided the experimental results for contact studies. The experiment done by Tabor[7] on indentation revealed the physical insight into the surface interactions. Johnson[24], in the mid-1990's, proposed a model dividing the event of impact into a fully elastic phase and fully plastic phase. His further study[48] demonstrated that the restitution phase of impact will always have a reverse plastic flow rather than the purely elastic recovery, and this was backed

by Tabor's experiment. Furthermore, many theoretical models were proposed improving the Hertz theory, but achieving a closed form solution addressing plasticity, instantaneous velocity, and instantaneous force was a problem. In the early 1990's, Stronge[56],[55] came up with the energy approach in order to study the event of impact and introduced a new coefficient of restitution based on energy principles. In the late 1990's, with the advent of the finite element method(FEM), the study of contact got more focused on micro-indentation[2] and nano-indentation[42]. Many models were put forth to predict these factors, which were unable to solve through traditional closed form theories. Tabor's experimental results served as a reference for many FEM models. The early FEM indentation models were based on minimal computational time and effort. Hardy[20] et.al. in 1971, Kral et.al [32] in 1993, and Ogbonna et.al.[43] in 1995 studied these indentation models in FEM; their work concentrated on achieving the appropriate mesh and effective computational time for the analysis to validate the results of Tabor experiments. Mesarvic and Fleck[41] in 1999 studied the Brinell indentation as a part of a large computational study. Since the early 2000's, more sophisticated models have been designed with increased computational power. The models formulated were more robust, and many scholars created empirical formulations to predict the contact force, deformation or indentation, and other behaviors of impact based on the simulator results. Yo Komvopoulos [64] developed a new formulation for the indentation of homogeneous and layered material using FEM. Kogut and Komvopoulus (the KK model) [30] came up with an interactive approach through FEM simulation for determining the indentation, contact force and plastic deformation of the base. These results are also validated by his experiments. Later Kogut and Elsio (the KE model) [29] presented a flattening model with a new empirical formula on elastic-plastic contact of a sphere on a rigid flat surface. Komvopoulos and Ye [31] were the first to model a 3-D contact analysis of impact with a non-homogeneous flat surface, accounting for the roughness of the surface. Jackson and Green (the JG model)[23] in 2004 presented a flattening model; they used an axisymmetric 2D model of an elastic-perfectly plastic sphere in frictionless contact with a rigid flat surface.

The resulting numerical data was fitted to capture deformations from purely elastic to fully plastic conditions, and in turn led to a new empirical formulation based on Poisson's ratio, elastic modulus, and yield strength of the material under impact. Brake[11] developed a new model to determine the contact force and the area of contact. He further divides the event of impact into 4 phases:fully elastic, elasto-plastic, fully plastic, and restitution. In more recent studies, Alcala et al. [4] developed a model to determine the mechanical properties of the material under impact considering the effect of friction, the strain hardening rate, and contact radius. Furthermore, in 2014, Hamid, Marghitu and Jackson [17],[19] studied all the models mentioned above and formulated a modified version of a JG model to measure the indentation on the impact base, using the experimental and FEM results. Recent studies by Kefie and Jackson [22] and Yang, and Green [61] regarding contact analysis focused on the 3D simulations and FEM parametric analyses of line and surface contact rather than point contact. The effect of friction and hardening are studied for specific cases of plane stress and plane strain. These studies are imitated to specific cases, and the present study is an attempt to generalize and validate the dynamic 3D simulation of the contact.

1.2.1 Indentation models

The basic formulation of the Hertzian Contact Theory (spherical indenter) of the indentation model is described here.

The mean contact pressure (P_m) of the contact is defined as

$$P_m = \frac{P}{a} \tag{1.12}$$

where a is contact area and P is the normal load, and the truncated contact area $a‘$ is defined as

$$a‘ = \pi\,(r‘)^2 = \pi\,\delta\,(2\,R - \delta) \tag{1.13}$$

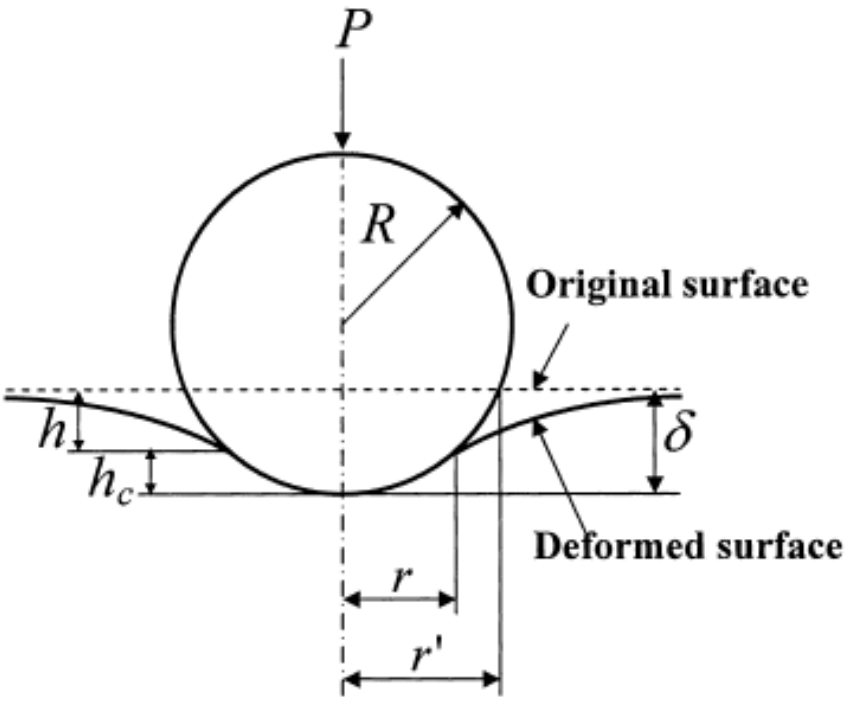

Figure 1.1: A schematic illustration of a spherical indentation.

which is given as a function of the radius of the truncated contact area, r‘ and the indentation δ of the rigid sphere on a flat surface.

Based on Hertz theory, the reduced modulus of elasticity is given by

$$E = \left[\frac{(1-{\nu_1}^2)}{E_1} + \frac{(1-{\nu_2}^2)}{E_2}\right]^{-1} \tag{1.14}$$

where E is the reduced modulus of elasticity. For the elastic phase the indentation δ is;

$$\frac{\delta}{r‘} < 1.78\left(\frac{E}{Y}\right)$$

after which the material starts to yield.

The deformation δ of the flat can be written as a function of contact load and material properties

$$\frac{P_m}{Y} = \frac{4\sqrt{2}}{3\pi}\frac{E'\delta}{Yr‘} \tag{1.15}$$

$$\frac{a`}{a} = 2$$

Komvopoulus Kogut Model (*KK Indentation Model*) [30]

The KK Indentation model divides the event of impact as 3 phases: the elastic phase, the elasto-plastic phase, and the restitution phase. The elastic phase is governed by the Hertz contact theory. Based on the empirical results, and FEM analysis interface between the elastic phase and the elastic-plastic phase is formulated as a constant ratio between the contact pressure and the yield strength of the material (see Equation 1.16), or expressed as a critical deformation (see Equation 1.17) at which point yielding is initiated.

In the elastic-plastic phase, the expression for contact pressure and contact area are derived by using FEM simulation results.

$$\frac{P_m}{Y} = 0.839 + ln\left[\left(\frac{E}{Y}\right)^{0.656}\left(\frac{\delta}{r'}\right)^{0.651}\right] \tag{1.16}$$

$$\frac{a'}{a} = 2.193 + ln\left[\left(\frac{E}{Y}\right)^{0.394}\left(\frac{\delta}{r'}\right)^{0.419}\right] \tag{1.17}$$

Further, by correlating these 2 expressions, a dimensionless contact load is defined as

$$\frac{P}{a'Y} = \frac{0.839 + ln\left[(E/Y)^{0.656}(\delta/r')^{0.651}\right]}{2.193 + ln\left[(E/Y)^{0.394}(\delta/r')^{0.419}\right]} \tag{1.18}$$

The restitution phase is described as the unloading behavior or recovery phase, and the plastic or permanent deformation is called the residual impression, (δ_r). The recovery of the elastic deformation of the material is characterized by the change in the displacement at the center of indentation, $E_{R\delta}$,

which is defined as

$$E_{R\delta} = \frac{\delta_i - \delta_r}{\delta_i} \tag{1.19}$$

where δ_i is the maximum indentation on the base in the event of impact, δ_{max}. Also, the ratio of the elastic energy released upon unloading to the total input energy during loading is defined as

$$E_{RE} = \frac{\int_{\delta_f}^{\delta_i} P(\delta) * d\delta}{\int_{0}^{\delta_i} P(\delta) * d\delta} \tag{1.20}$$

Using curve fitting for these simulation results, the ratios are expressed in terms of the mechanical properties of the material, as shown below.

$$E_{R\delta} = 0.591 \left(\frac{E}{Y}\right)^{-0.156} \tag{1.21}$$

$$E_{RE} = 0.616 \left(\frac{E}{Y}\right)^{-0.176} \tag{1.22}$$

Thus, by rearranging the terms we can get the expression for permanent deformation on the impact point of the base

$$\delta_r = \delta_i \left[1 - E_{R\delta}\right] \tag{1.23}$$

Brake Indentation Model[11]

Brake's model formulated contact behavior of indentation by accounting for friction and the strain hardening effect. Brake's model divides the impact into an elastic phase and an elastic-plastic phase. In his study, a transitionary function is used to define the behavior of impact with 9 practical assumptions applied to bound the function for one realistic solution. The elastic phase is again governed by the Hertz Contact Theory, and indentation at the point of the initiation of yielding is given by

$$\delta_y = \frac{r}{F(\nu)} \left(\frac{\pi\,\sigma_y}{2\,E}\right)^2 \tag{1.24}$$

In the elastic-plastic phase, i.e., when ($\delta > \delta_y$), nonlinear strain hardening coefficient H and exponent n are used to account for the effect of hardness of the material during the event of impact.

Contact compliance after the inception of yielding is expressed using the transitionary function

$$\begin{aligned} F =& sech\left((1+n_\epsilon)\,\frac{\delta-\delta_y}{\delta_p-\delta_y}\right)\,\frac{4}{3}\,E\,\sqrt{r}\delta^{3/2} \\ &+\left(1-sech\left((1-n_\epsilon)\,\frac{\delta-\delta_y}{\delta_p-\delta_y}\right)\right)\,p_0\,\pi\,\frac{a^n}{{a_p}^{n-2}} \end{aligned} \tag{1.25}$$

, and where $p_0 = Hg10^6$ is the contact pressure for a fully developed plastic flow without strain hardening and

$H = \left(\frac{2}{H_s} + \frac{2}{H_f}\right)^{-1}$ is the Brinell's Hardness of the material and $n_\epsilon = n-2$ is the strain hardening exponent where n is the Meyer's hardening exponent, here a_p is the characteristic contact radius of the plastic phase is expressed as;

$$a_p = \left(\frac{3p_0}{4E}2^{n/2}\pi\,r^{(n-1)/2}\,{\delta_y}^{(n-3)/2}\right)^{1/(n-2)} \tag{1.26}$$

and the indentation at the end of elastic-plastic phase is expressed as

$$\delta_p = \frac{{a_p}^2}{2R} \tag{1.27}$$

The restitution or unloading phase is assumed to be elastic in nature and is therefore governed by the Hertz theory. At the end of loading phase, a deformed radius of curvature r' and permanent indentation δ' is sustained in the body due to plastic deformation. δ', the permanent deformation and r', deformed radius of curvature, is expressed as function of maximum deformation δ_m and maximum contact force F_m during the loading phase.

$$\delta' = \delta_m \left(1 - \frac{F_m}{4/3E\sqrt{r}{\delta_m}^{3/2}}\right) \tag{1.28}$$

Similarly, the radius of the curvature of unrecoverable indentation is expressed as

$$r' = \frac{{F_m}^2}{(4/3E)^2(\delta_m - \delta')^3} \tag{1.29}$$

1.2.2 Flattening models

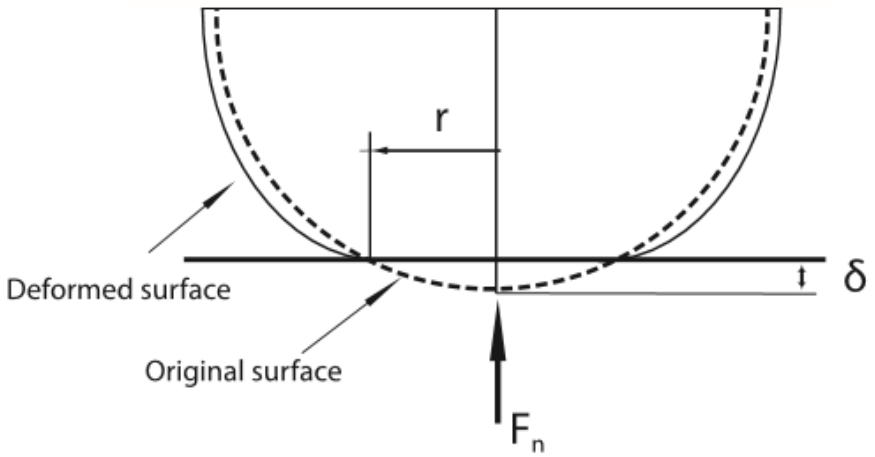

Figure 1.2: A schematic illustration of an elastic-spherical surface impacting on a rigid-flat surface

Jackson Green Model[23]

The Jackson Green model uses a 2D axisymmetric finite element model of an elastic-perfectly plastic sphere in frictionless contact with a rigid flat surface. Figure 1.2 shows the schematic representation of the flattening model. Here, the elastic hemisphere is in contact with a flat surface with a static contact load F_n. The event of the contact(compression) is divided into elastic and elastic-plastic phase. The deformation δ is in an elastic region until the inception of yielding; the point where material starts to yield is defined as the critical interface, δ_c of deformation.

The JG model provids an analytical expression for critical deformation by using the von Mises yield criterion. δ_c is expressed in terms of yield strength of the hemisphere in

$$\delta_c = \left(\frac{\pi\, C\, Y}{2\, E}\right)^2 R \tag{1.30}$$

, and here, C is the yield strength coefficient defined as the ratio of the maximum contact pressure to the yield strength of the material

$$C = \frac{P_{oy}}{Y} = 1.295\, e^{(0.736\nu)}. \tag{1.31}$$

, and P_c is the critical load to initiate yielding during the impact

$$P_c = \frac{4}{3}\left(\frac{R}{E}\right)^2 \left(\frac{C}{2}\,\pi\, Y\right)^3 \tag{1.32}$$

In the elastic plastic phase, an empirical formula is developed using FEM simulation results of various interfaces of impact with different material properties and spherical geometric parameters. The effect of hardness at the high interface of the impact is isolated by defining a ratio of average pressure H_G to yield strength Y. Thus, the change in the hardness with the amount of contact interface is established. Further fitting those FEM results with the

Weibull function, an expression relating the mechanical properties with the contact area and deformation has been formulated as

$$\frac{H_G}{Y} = 2.84\left[1 - e^{\left(-0.82(a/R)^{-0.7}\right)}\right] \tag{1.33}$$

$$\frac{a}{R} = \frac{\pi\, C\, e_y}{2}\left[\delta^*\left(\frac{\delta^*}{\delta_t{}^*}\right)^B\right]^{1/2} \tag{1.34}$$

The restitution phase is formulated in the further study of the JG model [23] as the model evolved with the analysis of more FEM simulation results using curve fitting models to predict the empirical formula for the plastic deformation, δ', and rebound velocity (COR) of the elastic-perfectly plastic sphere.

$$\delta' = \delta_m\left(1.02\left[1 - \left(\frac{\delta_m/\delta_c + 5.9}{6.9}\right)^{-0.54}\right]\right) \tag{1.35}$$

.

Modified Jackson Green Model[19]

The FEM model, developed by Hamid, Jackson and Marghitu [17, 19] is known as a modified JG model and is also based on the 2D elements with asymmetric conditions. The modified JG model has evolved from studies of all the previous indentation and flattening models where one of the bodies under impact was assumed to be rigid. In this model, both the surfaces undergo the impact elasto-plastically. By comparing and contrasting with many prominent FEM models and validating them with the experimental results, a successful attempt has been made to explain and provide a transition between the indentation and flattening models and to predict the contact force, permanent deformation and rebound velocity during impact on both surfaces.

This study follows the same theory of the JG model, and hence, for the elastic phase of the impact, the expressions remain the same for contact force and deformation. For the

elasto-plastic phase, a new term is expressed as the ratio S_y of yield strength of sphere S_{ys} and flat surface S_{yf} below:

$$S_y = \frac{S_{ys}}{S_{yf}} \tag{1.36}$$

,

which is used to formulate the transitioned normalized hardness expressions accounting for changes in hardness in both surfaces, and, in turn, the contact force and deformation. The restitution phase follows the Hertz theory. The expression given below is for the permanent deformation (δ_c) and contact (P_r) force, based on empirical formula to describe the deformation on both the surfaces undergoing the impact.

$$\delta' = 0.8\,\delta_m \left[1 - \left(\frac{\delta_m/\delta_c + 5.5}{6.5}\right)^{-2}\right] \tag{1.37}$$

where δ_c is the permanent deformation after unloading phase, δ_m is the maximum deformation at the compression phase.

$$P_r = \frac{4}{3} E R'^{0.5} (\delta - \delta_r)^{1.5} \tag{1.38}$$

The restitution phase is governed by Hertz theory as in a JG model, so the expressions for deformation and contact load remains the same for both bodies. The respective maximum and critical deformation can be used to approximate the permanent deformation on either spherical or flat surfaces.

1.3 Theory and historical background on the impact of fluid-coupled tubes

Impulsive loading of the fluid-filled tubes and the resulting fluid-structure interaction has been studied extensively. The studies on classical water hammer events deal with the normal impact and effect of FSI due to the coupling of flexural waves[47, 65] in shells with the pressure shock waves[46] in the fluid propagating perpendicular to the surface of the shell.

The theory of stress wave propagation in the fluid-filled tube walls have been experimentally validated by Korteweg and Joukowsky. Further studies on this were done by Skalak[57] to account for the acoustic model and axisymmetric modes of deformation caused by the radial oscillation of the tube coupled with the motion of the fluid. Numerical and experimental studies have been done to describe the folding mechanism of deformation and estimate the energy absorbing characteristics of the fluid-filled thin cylinders undergoing axial impact. Early finite element analysis of fluid-structure interaction illustrating the sloshing effect on liquid structures has been studied by S.SubhashBabu and S.K.Bhattacharyya[8] The present study is focused on the development of a finite element technique to calculate the sloshing displacement of liquid and pressure developed due to such sloshing. This scheme was extended to study the coupled effect of sloshing and container wall movement due to change in the liquid pressure. Subsequently, in both civil and military fields, research and experimentation on the fluid–structure interaction of water-filled tanks and cylinders during the impact were carried out. Analysis of the crashworthiness of fuel tank for helicopter by utilizing the finite element method (FEM) were done by Marco Anghileri[6], Xianfeng Yang[63] and many researchers. The dynamic response of the drop test of a fuel tank is a representative fluid–structure interaction (FSI) problem, which is extremely complex owing to the strong nonlinearity and large deformation. It can be simulated in many different methods. Finite Element Eulerian, Lagrangian, Arbitrary Lagrangian Eulerian (ALE), and Smoothed Particles Hydrodynamics (SPH), etc. Zhang Y.T.[68]et.al. have worked extensively on each of these methods, and SPH methods have been proven to be the most effective in simulating the FSI events like drop testing fluid-filled tanks. Comparing with ALE, SPH is said to be more accurate but is computationally more expensive than other methods. ALE can be used to analyze the ways flexible fluid-filled containers change shape on impact. The limiting factors of water hammering and the bulking of the structures as a result of impact under the influence of fluid are presently studied. The deformation and stress response of the structures over time are analyzed to model the effect of fluid during the event of impact.

In the present study, a 3D explicit dynamics method is used to analyze the impact behavior of the fluid-filled tube during and after the event of impact. An explicit dynamic uses an SPH reference frame for meshing and analysis. In this module of ANSYS, solid bodies can be assigned either a Lagrangian reference frame or a Eulerian reference frame. The reference frames can be combined in the simulation to allow the best solution technique to be applied to each type of material being modeled. During the simulation, bodies in both the Eulerian and Lagrangian reference frames will automatically interact with each other, establishing a fluid-structure interaction. Even though it is computationally expensive for present computational power, with future advancements in high-speed computing and parallel processing, the simulations with these methods will be more relevant going forward. An attempt is made in this regard to analyze the impact response of fluid-filled tubes and effect of natural frequency in the event of the impact using explicit dynamics.

Chapter 2

Modal analysis of fluid-coupled thin structures

In the paper [40] published by Amabili [5].et.al., the effect of fluid to enhance the non-linear behavior of the shell vibration, and the importance of non-linear analysis in fluid-filled shells are discussed in detail. In the normal engineering field, such an analysis for all the coupled systems is cumbersome, even with the help of FEM analysis. An important problem for a structure-acoustic analysis using FEM is that the number of degrees of freedom easily becomes very large when solid element SOLID-186 is used to represent structures to achieve a symmetrically coupled matrix formulation with the fluid element FLUID-220. Another problem associated with fully symmetrical coupled matrix formulation is the incompatibility of shell elements in modeling the symmetric matrix of coupled motion of thin-wall and fluid. But SHELL-63, a structural shell element will couple with fluid element FLUID-30 with the lack of symmetry in the system of equations and coupling matrix. In all these methods, the large bandwidth of the system matrices and the coupling matrix add up to a long computational time. It is more productive to predict the coupling factor[see Equation 2.21] in the structural design process rather than spend a significant amount of time monitoring the modal characteristics of every coupled structure(cylinder) if other dynamics properties of the fluids are not of practical interest. However, predicting the natural frequency of the coupled structure is a complicated mathematical problem. The solution is only calculable using higher order equations, and theoretical solutions are restricted to specific models and boundary conditions. However, generalizing the prediction for coupled modal frequencies of the cylinders for all the boundary conditions and for all possible vibration modes in a complicated structure is still not practical. Therefore, for a specific familiar model and for a specific range of structural and fluid properties, a parametric study can be done to simplify

the relationship between the coupled and uncoupled model to obtain an approximate solution to the modal frequencies of the coupled structure from the data of the uncoupled analysis. This saves a lot of computational time in the static structural design where the vibrational characteristics are not the primary objective but cannot be neglected. An attempt is made in this regard to achieve a feasible approximation of the first few natural frequencies of the thin cylinders under the influence of dense fluids, such as water, for a given natural frequency of these cylinders(empty).

2.1 Finite element formulation

A number of finite element formulations have been proposed for acoustic fluids in the analysis of fluid-structure interaction problems, namely the displacement formulation, the displacement potential and pressure formulation (Morand and Ohayon), and the velocity potential formulation (Everstine, Olson and Bathe)[44]). The displacement formulation has received considerable attention because it does not require any special interface conditions or new solution strategies and because of its potential applicability to the solution of a broad range of problems. Figure 2.1 illustrates the classical modal behavior of the cylinders, where the natural frequencies increase with the mode number, but the first few natural frequencies correspond to higher modes and the first few modes occur at higher frequencies. Hence there is an initial dip in the natural frequencies compared to the mode number curve. This dip is governed by the geometry of the cylinder under analysis. The details of the topic are explained in sections ahead. In the finite element formulation, a system of equations describing the motion of the system is developed, with the number of equations equal to the number of degrees of freedom introduced in the finite element discretization. For the structure-acoustic system, the structure is described by the differential equation of motion for a continuum body assuming small deformations, and the fluid is described by the acoustic wave equation. Coupling conditions at the boundary between the structural and fluid domains ensure the continuity in displacement and pressure between the domains.

The governing equations of each domain based on their boundary conditions are:

$$\begin{aligned} \text{Structure} &: \tilde{\nabla}^T \sigma_S + b_S &&= \rho_S \frac{\delta^2 u_S}{\delta t^2} \\ \text{Fluid} &: \frac{\delta^2 p_F}{\delta^2 t} - c^2 \nabla^2 p_F &&= c^2 \frac{\delta q_F}{\delta t} \\ \text{Coupling} &: \vec{\sigma_S} \vec{n} + p\vec{n} &&= 0 \\ &: \vec{n} \cdot \vec{u_S} - \vec{n} \cdot \vec{u_F} &&= 0 \end{aligned} \tag{2.1}$$

where;

u_S, u_F = Displacement of solid and acoustic fluid; b_S = Body force

p_F = Pressure field in the acoustic domain; σ_S = Solid stress tensor

n = Outward normal unit vector of fluid domain; q_S = Inertia force

$$\tilde{\nabla}^T = \begin{bmatrix} \delta/\delta x1 & 0 & 0 \\ 0 & \delta/\delta x2 & 0 \\ 0 & 0 & \delta/\delta x3 \\ \delta/\delta x2 & \delta/\delta x1 & 0 \\ \delta/\delta x3 & 0 & \delta/\delta x1 \\ 0 & \delta/\delta x3 & \delta/\delta x2 \end{bmatrix}$$

To arrive at the finite element formulation for these individual domains, a weak form of the differential equations is derived[13, 50, 49, 51, 52, 53]. The finite element formulation is formed by using the integral of the governing equation with the structural domain. Through the derivation of the above function, using the shape function, displacement domain, and weight function, the finite element structural domain can be formulated as being the following:

$$\int N_S^T \rho_S N_S dV \ddot{d}_S + \int (\tilde{\nabla} N_S)^T D_S \tilde{\nabla} N_S dV d_S = \int N_S^T t_S dS + \int N_S^T b_S dV \tag{2.2}$$

This governing system of equations can be written as the following;

$$M_S\ddot{d}_S + K_S d_S = f_F + f_b \tag{2.3}$$

where;

$$M_S = \int N_S^T \rho_S N_S dV; \qquad K_S = \int (\tilde{\nabla} N_S)^T D_S \tilde{\nabla} N_S dV$$

$$f_F = \int N_S^T t_S d_S; \qquad f_b = \int N_S^T b_S dV$$

N_S = Finite element shape function of structure; D_S = Constitutive matrix

d_S = Displacement matrix; b_S = Inertia matrix

Similarly, considering the governing equation of in-viscid acoustic fluid, a weak finite element formulation can be done by integrating the time derivative of the governing equation of fluid over volume[50, 49, 51, 52, 53].

Expressing the pressure field of the acoustic fluid as the shape function and weight function, a finite element of governing equation can be formed for fluid domain, as noted below.

$$\int N_F^T N_F dV \ddot{p}_F + c^2 \int (\tilde{\nabla} N_F)^T \tilde{\nabla} N_F dV p_F = c^2 \int N_F^T \nabla p_F n_F dS + c^2 \int N_F^T \frac{\delta q_F}{\delta t} d_V$$

This governing equation can be written as following;

$$M_F\ddot{p} + K_F P = f_q + f_S \tag{2.4}$$

where;

$$M_F = \int N_F^T N_F dV; \qquad K_F = c^2 \int (\nabla N_F)^T \nabla N_F dV$$

$$f_S = c^2 \int N_F^T n_F^T p dS; \qquad f_q = c^2 \int N_F^T \delta q / \delta t dV$$

N_F = Finite Element Shape Function of Acoustic Fluid

Now, the coupled structure-acoustic system can be defined at the interface of the fluid and structure. At the boundary, the fluid to the structural nodes should have same displacement and pressure in a normal direction. Hence, the displacement and pressure boundary conditions can be written as the following:

$$\begin{aligned} \vec{\vec{\sigma_S}}\vec{n} + p\vec{n} &= 0 \\ \vec{n} \cdot \vec{u_S} - \vec{n} \cdot \vec{u_F} &= 0 \end{aligned} \tag{2.5}$$

Now the coupling can be introduced in the form of force $f_S$and f_F by relating pressure and the acceleration of the fluid to the structural domain at the boundary. Structural force f_F is related to both the stress and pressure acting on the structure and fluid as shown the following equation:

$$f_F = \int N_S^T n N_F d_S P_F \tag{2.6}$$

Similarly, the force acting on the fluid f_S is related to the acoustic fluid pressure and stress in the followi

$$f_S = -\rho_0 c^2 \int N_F^T n^T N_S d_S \ddot{d}_S \tag{2.7}$$

where:

$p_F = N_F P_F$; p_F = Pressure field

P_F = Nodal pressure; N_F = Finite element shape function of fluid domain

The structure – acoustic problem in the finite element method can be expressed as;

$$\begin{bmatrix} M_S & 0 \\ \rho_0 c^2 H_{SF}^T & M_F \end{bmatrix} \begin{bmatrix} \ddot{d}_S \\ \ddot{P}_F \end{bmatrix} + \begin{bmatrix} K_S & -H_{SF} \\ 0 & K_F \end{bmatrix} \begin{bmatrix} d_S \\ P_F \end{bmatrix} = \begin{bmatrix} f_b \\ f_q \end{bmatrix} \tag{2.8}$$

by defining a Spatial Coupling Matrix with the equation:

$$H_S F = \int N_S^T n N_F dS \tag{2.9}$$

2.2 Validation of the finite element method used for analysis

In order to examine the feasibility and accuracy of the proposed iterative scheme, a benchmark problem has been solved and compared with the existing literature. In the book 'Sound Structure and their Vibration' by Miguel C. Junger[27], there is an intensive discussion about the coupling of structure and fluids at different frequency ranges.

2.2.1 Junger's approach on fluid-structure coupling[27]:

Consider an elastic structure excited by N Force F_j immersed in an acoustic fluid and hence exposed to radiation loading in the form of pressure as in Equation 2.10 below.

$$p(R_j) = \int \dot{\omega}(R_0) G(R_j|R_0) dS(R_0). \tag{2.10}$$

This is the broad explanation of the coupled space of fluid and structure [see Equation 2.2.1]. With field points R_j located on the structure-fluid interface. The acoustic surface pressure now contributes to the oscillatory force applied to the structure and must therefore be accounted for when computing the dynamic response of the structure. The dynamic response of the submerged structure can be represented as

$$\dot{\omega}(R_k) = -\int \gamma(R_k|R_j)[\int_S \dot{\omega}(R_0) G(R_j|R_0) dS(R_0)] dS(R_j) + \sum_{j-1}^{N} F(R_j)\gamma(R_k|R_j). \tag{2.11}$$

where;

R_j = Field point; R_0 = Position vectors of the structure

G = Green's Function; $\dot{\omega}$ = Angular velocity distribution

p = Pressure; γ = Drive-point mobility or transfer mobility

Moving forward to the specific system with which we are interested in, let us consider a fluid-filled spherical shell, as there is advantage of spherical symmetry in the system,

analytically closed form solution can be obtained for the restricted boundary conditions. The pressure field and normal modes of fluid-filled spherical shells are factors which can be mathematically formulated. The pressure, p(a), acting on the inside of a spherical container vibrating uniformly is given by the following equation:

$$p(a) = \frac{i\rho ckaW}{ka\cot ka - 1} \tag{2.12}$$

where;$\dot{W} =$ Velocity amplitude; $a =$ Radius of curvature; $k =$ Wave number

Restricting the analysis to the $n = 0$ mode or breathing mode of vibration. The dimensionless frequency will be given by the equation,

$$[-\Omega^2 + 2(1+\nu)]W_0 = \frac{a^2 p(a)}{\rho_S c_p^2 h} \tag{2.13}$$

The dynamic stiffness of the spherical wall can be obtained by the formula

$$k_0 = \frac{\rho c^2 k^2 a^2}{a(1 - ka\cot ka)} \tag{2.14}$$

Additionally, the pressure can be expressed as

$$p(a) = -k_0 W_0 \tag{2.15}$$

$$2(1+\nu) = \Omega_0^2 \tag{2.16}$$

Hence, the characteristic equation of the fluid filled sphere is

$$\frac{\rho_S c_p^2 h}{3\rho c^2 a}(\Omega^2 - \Omega_0^2) = \frac{k_0 a}{3\rho c^2} \tag{2.17}$$

where;

c_p = Phase velocity of the compressible wave

This is a transcendental equation, because k_0 is frequency dependent. Thus, this equation has a series of solutions for a single mode. Calculations were performed for the following structure and fluid properties:

Structure : $Steel$

Young's Modulus : $2.1\text{e}^{11} Pa$

Poisson's Ratio : 0.28

Fluid : $Water$

Density : 1000 kg/m^3

Sonic Speed : 1484 m/s

For a water filled steel sphere of radius 1 m;

1^{st} breathing mode = 928 Hz

2^{nd} breathing mode = 1653.18 Hz

3^{rd} breathing mode = 2322.66 Hz

2.2.2 The finite element method

Now, in order to validate and verify the FEM model, the structure and fluid elements are coupled at the intersection. Numerical modeling is done using ANSYS- APDL 17.1. Two means of FEM modeling are shown that represent the fluid-structure coupling:

3D Elements : The structures were modeled as a SOLID element-186 and fluid was modeled as Acoustic Element-230.

Shell Elements : The structures were modeled as SHELL-63 elements and fluid was modelled

as Acoustic Element-30.

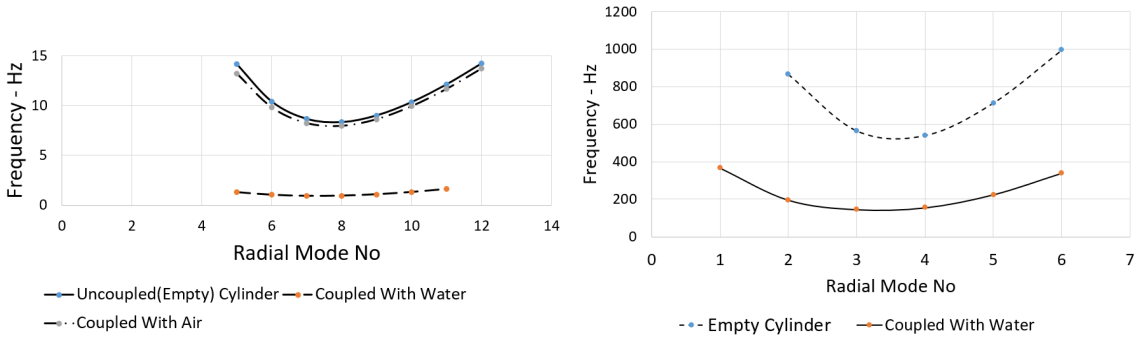

Figure 2.1: Natural frequency of coupled and uncoupled cylinders

Breathing modes refer to the vibrational modes associated with the flexural motion of the shell wall, such that the radial displacement is proportional to $\cos n\theta$ where $n = 0$, which corresponds to rotationally symmetric motion. Hence, a frequency response analysis is done by applying equal pressure over the spherical surface. At the breathing mode frequency, there is least resistance to all the nodal displacements in the normal direction as a response to the symmetric pressure over the surface of sphere. Thus, there will be a peak in the normal displacement of a given node at the breathing mode frequency; the corresponding normal displacement is plotted over the frequency for the outer surface nodes at $x = 0$ *and* $y = 0$ as observed in the graphs in Figures 2.3 and 2.4

The model in Figure 2.2 describes a sphere filled with fluid, and the nodes on the inner boundary of the sphere are coupled with the fluid elements inside. A pressure load is applied over the surface of the sphere. As that pressure acts on the surface of the sphere, the frequency response of the sphere with respect to the normal displacement of the surface is plotted as shown in Figures 2.3 and 2.4 . There is significant normal displacement at a specific frequency, which can be asserted as the breathing mode of the sphere. More precise values for the frequency were obtained by running the analysis in the close range of individual peaks.

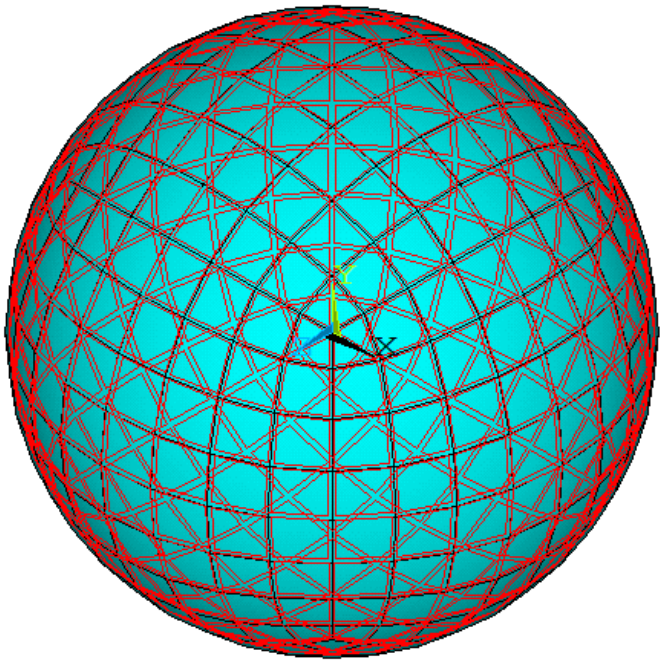

Figure 2.2: Sphere mesh

Table 2.1: Comparison with Junger's book - results

Breathing Modes of Coupled Sphere			
No.	Theoretical Frequency (Hz)	Solid Structural Element (Hz)	Structure as Shell Element (Hz)
1	971.2	868	871
2	1653.7	1533.7	1543
3	2322.6	2230	2252

The FEM results are similar to those of theoretical results in Table 2.1 using Junger's theory. The differences between eigenvalues are less than 5 percent. Thus, results apparently reflect that both FEM modeling methods are correct. It is also noted that for the uncoupled sphere, all the models provide $1400Hz$ as the breathing mode. On completing the analysis by using both symmetrically and unsymmetrically coupled matrix, it is evident that the accuracy of both the methods are agreeable given that the shell elements require a dense mesh to avoid numerical errors in the plots. For the given number of elements and mesh density, the symmetric matrix does solve it more efficiently, but meshing the structure is a

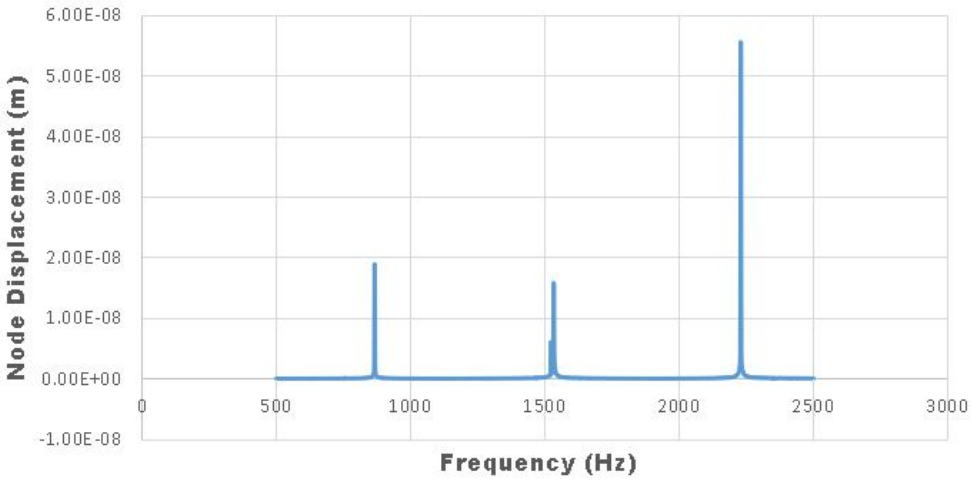

Figure 2.3: Frequency response of displacement of the sphere - solid element

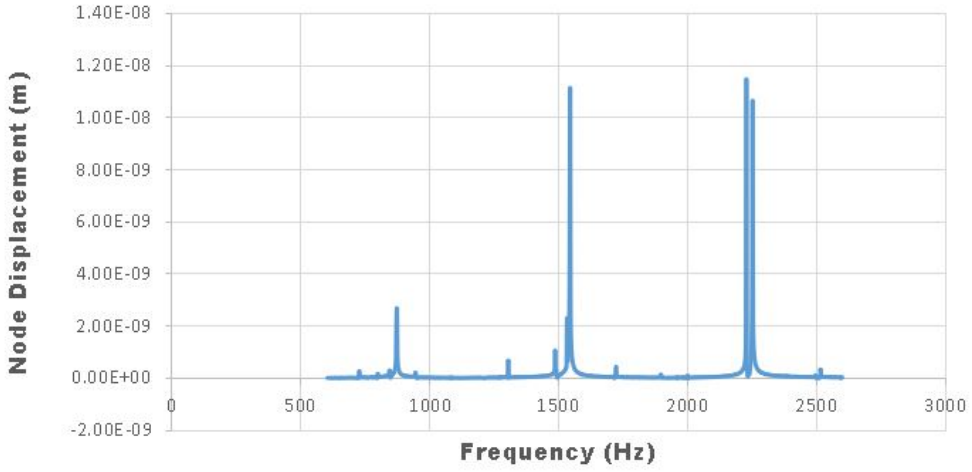

Figure 2.4: Frequency response of displacement of the sphere - shell element

meticulous and careful process. Shell elements are used for this parametric study as numerous interactions are completed by changing the model parameters for the analysis.

2.3 Modal characteristics of cylinders coupled with fluids:

In this section, an attempt is made to solve the fluid coupled structural vibration response. As previously stated, the modeling method had been proved right. The structure is represented by SHELL-63 elements and the fluid is represented by the Acoustics-30 element. Figure 3.1 shows the mesh of a closed cylinder with a 2 m radius and 5 m length with

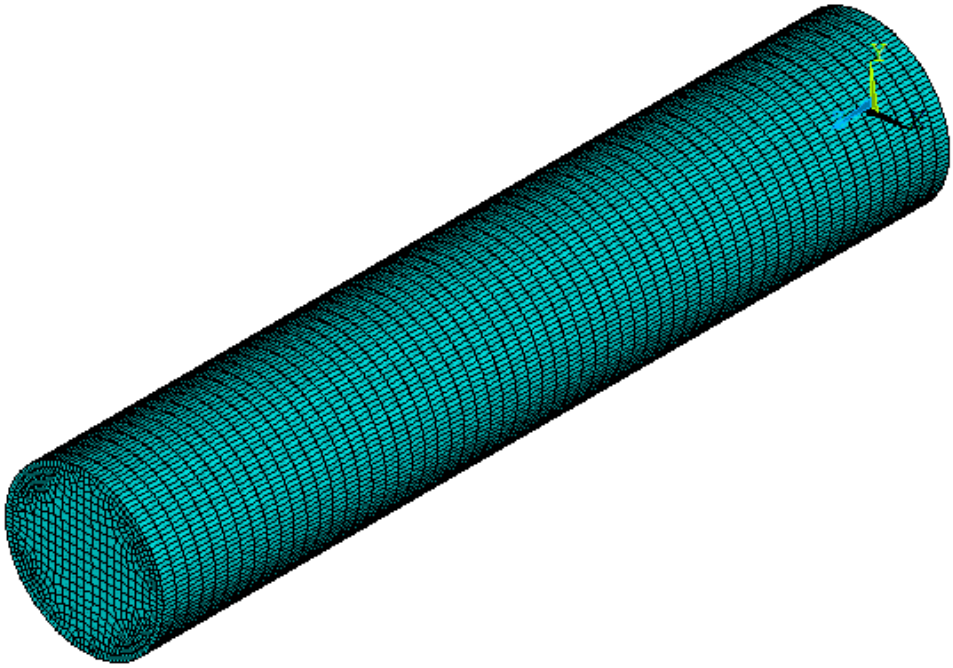

Figure 2.5: Cylinder coupled mesh

1 mm thickness containing fluid. The modal behavior of these structures is investigated by comparing coupled and uncoupled conditions.

The cylinder is designed as a thin and short cylinder to avoid more longitudinal or bending modes for the first 20 eigenvalues. The circumferential modes are of interest in this study; the reason for this is explained in further discussions.

$$Coupling\ Factor\ =\ \frac{Natural\ Frequency\ of\ Coupled}{Natural\ Frequency\ of\ Uncoupled} \tag{2.18}$$

The importance of coupling factors can be seen in Tables 2.3 and 2.4, where, for the empty cylinder, the first natural frequency is 25 Hz, at which point the cylinder undergoes a large displacement with least resistance. However, when it is coupled with water, the same state of vibration occurs at only 6 Hz. Thus, it should be noted that if a cylinder is installed in the dynamic system under the above stated condition, care must be taken to dampen this mode, which is over the range of 6 Hz to 25 Hz.

Table 2.2: Mode shapes

Radial Modes :- m=1		
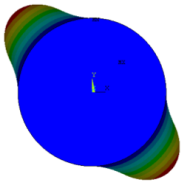 n = 2	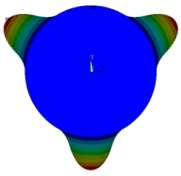 n = 3	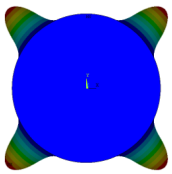 n = 4
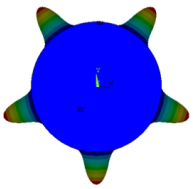 n = 5	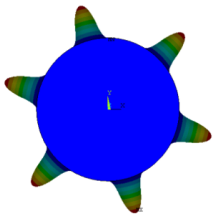 n = 6	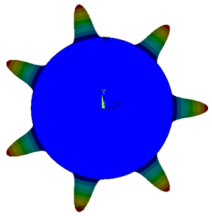 n = 7

Table 2.3: Radial modes and natural frequency of coupled and uncoupled cylinders (Hz)

Radial modes and natural frequency of couple and uncouple cylinder (Hz)			
Radial Mode No.	Empty Cylinder	Coupled with air	Coupled with water
3	36.797	36.388	8.343
4	25.665	25.442	6.5202
5	26.993	26.802	7.537
6	35.234	35.022	10.645
7	47.083	46.839	15.220

The analysis is done for cylinders with the following boundary conditions: 1) Fixed-Fixed boundary - where both ends of the cylinder are fixed in all directions.

2) Fixed-Free boundary, also known as a Cantilever cylinder, where one end is fixed and the other end is free.

Table 2.3 represents the natural frequency of the uncoupled cylinder-steel and the coupled condition with the fluids – air and water, respectively. It is evident that the coupling factor of the structure with air is negligible compared to that of water. It should be noted that the radial mode number and modal frequency are related as shown in the Figure 2.7. The curves show that the first few modes are not tabulated as they occur at a much higher frequency; those modes are outside of the parameters of this study, as we are concerned only

Table 2.4: Coupling factor of steel and aluminum coupled with air and water

Coupling factor of steel and aluminum coupled with air and water				
Radial mode No	Aluminum		Steel	
	Air	Water	Air	Water
5	0.837	0.053	0.934	0.091
6	0.857	0.058	0.943	0.099
7	0.873	0.062	0.949	0.107
8	0.886	0.066	0.953	0.114

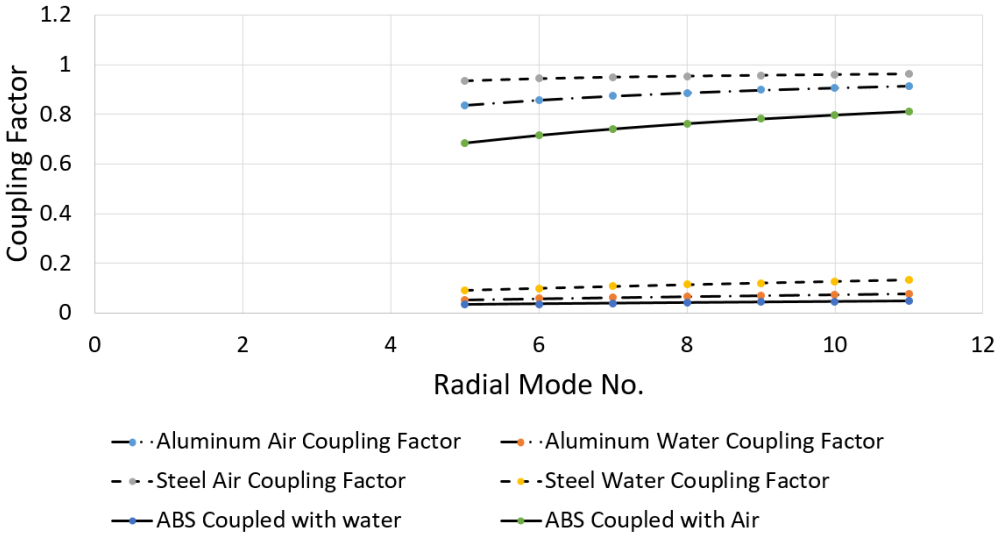

Figure 2.6: Coupling factor for weak and strong coupling

with the first few natural frequencies. There is still discussion on defining coupling factors as weak coupling and strong coupling, but in this case, it can be asserted that the air has a very weak coupling factor with respect to this structure. On the other hand, water can be treated as a strong coupling. Table 2.4 and Figure 2.6 represent the coupling factor of the same model with a different structural property – Aluminum. Comparing the results of these two structures, it is obvious that, for a given fluid, the coupling can be significant or insignificant based on the material property of the structure, so a soft structure such as a polymer, could have a coupling factor with high pressured air, which cannot be neglected. Hence, our area of interest concerns these strong couplings. However, the comparison of the empty and coupled natural frequency of the structure is complicated, as explained in the

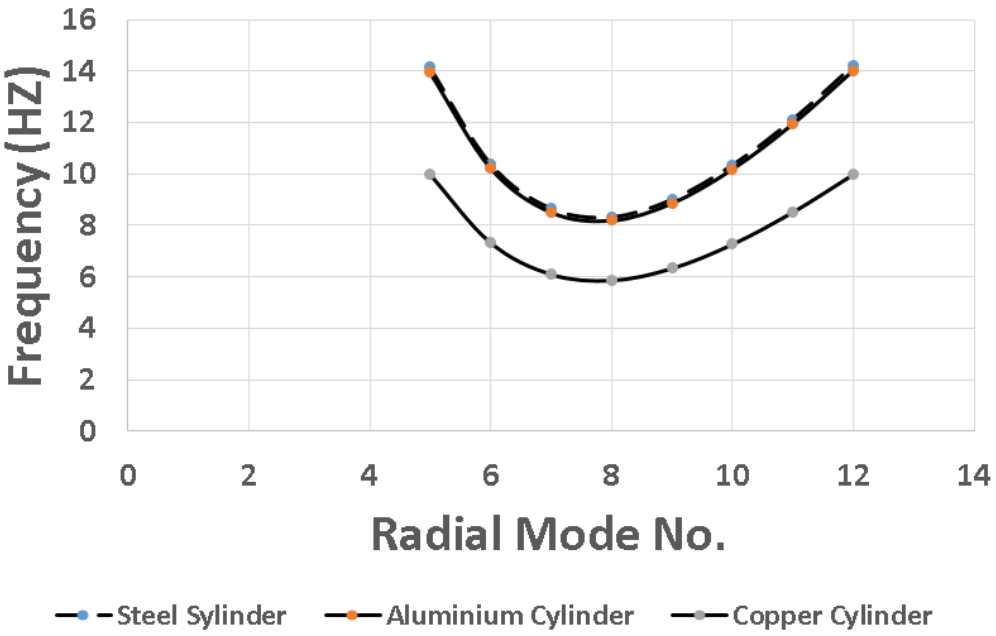

Figure 2.7: Natural frequency with different radial modes

previous chapter. The relationship between these frequencies is of complex, higher order differential equations.

An attempt is made here to relate these frequencies for a specific condition of dimensions, properties and boundary conditions for the cylinder and fluid. A parametric study is performed for each set of data input by modeling numerous models of varying factors, which are explained in detail in the coming chapters.

2.4 Parametric study of the modal characteristics of fluid coupled cylinders

To study the effect of the structural and fluid properties and geometric parameters of the cylinder on the coupling, individual parameters including the thickness, radius, and length, of the cylinder as well as the density of the structure and fluid are to be analyzed independently by keeping the other parameters constant. A specific parameter must be isolated to analyze the effect and significance of that parameter in the engineering design. The effects of these parameters with different measurements and materials are studied. Furthermore, the fluid properties contribute significantly for the coupling and, hence, drive the coupling

factor which we are attempting to predict. As described in the problem statement, the importance and non-linear behavior of fluid in a modal analysis of a cylinder is not practical to predict in a way which can be generalized to all fluids and structural conditions. Hence, the parametric study is confined to one fluid at a time to achieve more precise variations and better understand the dependencies of the other parameters over the coupling of the structure with the selected fluid. The fluid selected for the study in this paper is water. All the analyses carried out are with regard to the coupling characteristics of water with cylindrical structures.

2.5 Parametric study on the relation between modal frequencies of uncoupled, and water-coupled cylinders

Table 2.5: Properties of the structure and fluid described

Structure / Fluid	Property			
	Young's Modulus (E) (GPa)	Poisson's Ratio (μ)	Density (ρ) (kg/m^3)	Sonic Velocity (m/s^2)
Steel	210	0.28	8050	–
Aluminum	69	0.3	2070	–
Copper	117	0.28	8960	–
ABS	2.25	.23	1030	–
Water	–	–	1000	1484

Many finite element models are constructed, and normalizing techniques are used to help generalize the results for a specific range of models. For all models, the first 20 to 40 natural frequencies of the systems are calculated with the geometrical and structural properties mentioned in Table 2.5. In this analysis, some metal and polymer cylinders are examined. The cylinder dimensions are varied to get the desired mode shapes for the analysis on the effects of these variables on coupling. The following description summarizes the effects that these parameters have on coupled natural frequencies of the cylinder.

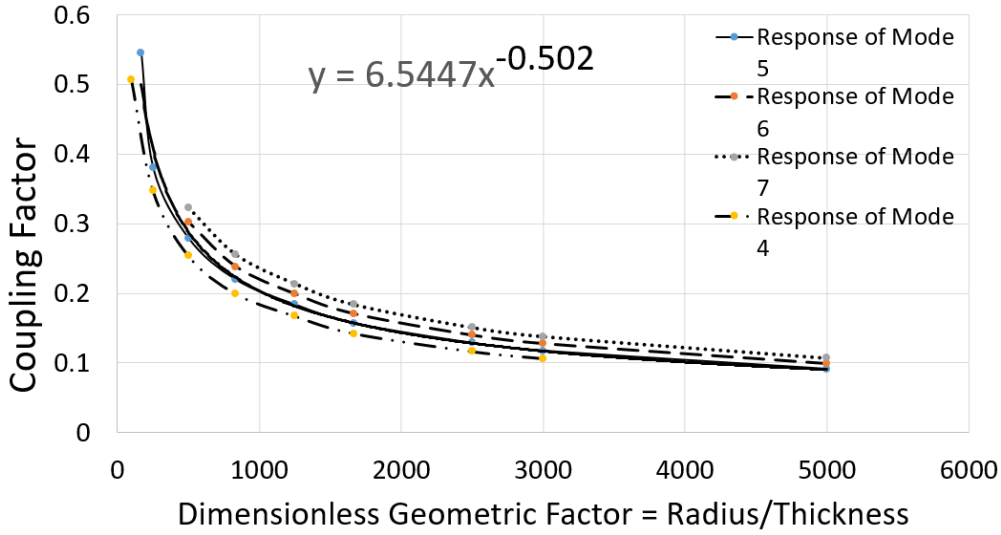

Figure 2.8: Effect of r/t on the coupling factor in a steel cylinder with fixed-end BC

2.5.1 Effect of the cylinder's thickness and radius on coupling

In this section, two geometrical parameters are considered as the design variables affecting the coupling factor. To show the effect of thickness and radius on coupling factor, a series of models were developed by considering a non-dimensional geometric factor defined as the ratio of radius to thickness of the cylinder. To obtain a clear variation with respect to thickness and radius in metal structures an ideal model is constructed with a very thin cylinder ranging in thickness from 0.1 mm to 5 mm and a large radius of 0.5 m. Thus, the dimensionless geometric ratio varies from 5000 to 50. For soft materials like ABS, the thickness ranges from 1mm to 5mm, and the radius ranges from 10 cm to 50 cm; here the ratio varies from 100 to 20. Figures 2.8, 2.9 and 2.10 show the relationship between the geometric factor and the change in the coupling factor of a system with different materials and radial mode numbers for both fixed ends and cantilever boundary conditions.

The modal used in Figure 2.8 is the steel cylinder of 5 m length coupled with water. As illustrated, the coupling factor decreases with the increase of the radius to thickness ratio. It should be noted that the effect of the coupling is stronger because ABS is a soft material, and it is not dense and stiff enough, compared to metals, to resist the interaction with

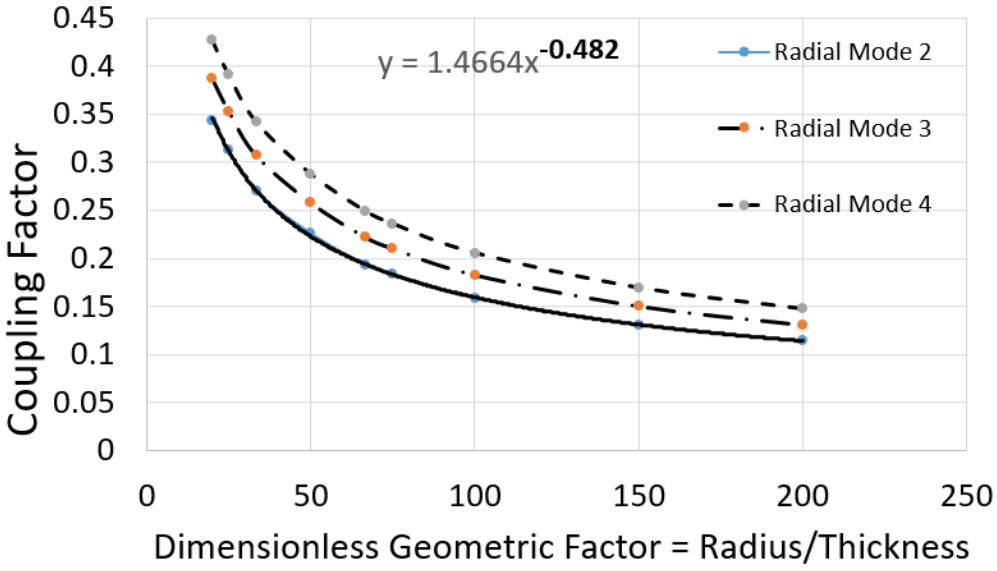

Figure 2.9: Effect of r/t on the coupling factor in an ABS cylinder with fixed-end BC

fluid motion. Thus, even thicker ABS cylinders coupled with the fluid vibration at much lower frequencies will have a stronger coupling compared to metals. Indeed, the variation for all the modes are same. The relation is shown in the Figure 2.8 as a power of -0.502. Similarly, another modal is built using ABS material and coupled with water. The relationship is shown in the Figure2.9. Also with the change in material property and boundary condition, the variation of coupling factor w.r.t geometric parameter is almost unchanged Figure 2.10. Therefore, the coupling factor is inversely proportional to the square root of the non-dimensional geometric ratio.

$$\begin{aligned} \text{Coupling Factor} &\propto \sqrt{\frac{1}{r/t}} \\ &\propto \sqrt{\frac{t}{r}} \end{aligned} \tag{2.19}$$

2.5.2 Effect of the structural material density on coupling

To investigate the effect of structural material density on the coupling factor, considering the properties of the material, models of the coupled cylinders were created with different

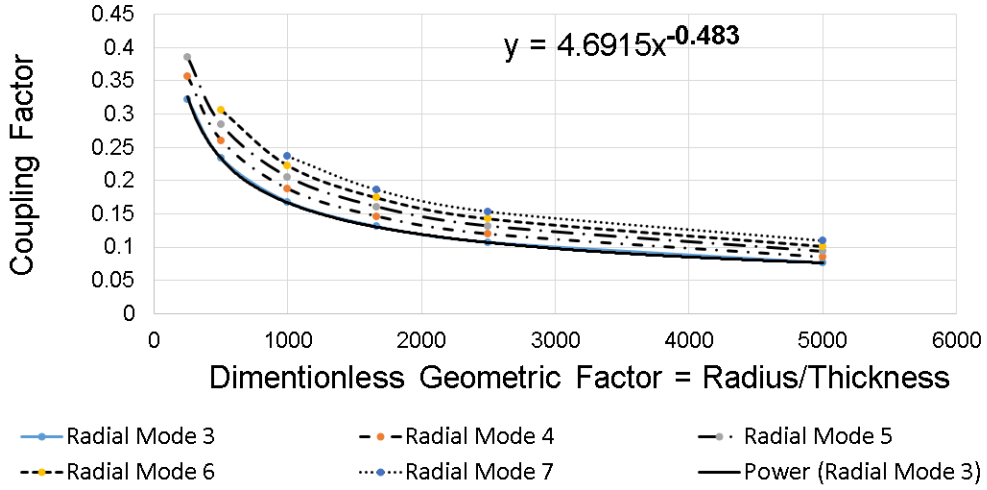

Figure 2.10: Effect of r/t on the coupling factor in a steel cylinder with cantilever-end BC

materials with varying densities. The coupling factor is calculated for same modes at a time. Figure 2.11 and 2.12 show the effect of structural density on the natural frequencies (coupling factor) of the water-coupled cylinder with the r/t ratio of 1000. Of course, an increase in the radial modes number leads to an increase in coupling frequency and vice versa, but it is evident that the variation of the coupling factor is also same for all the modes. Moreover, it is also obvious that the denser structural materials will have weak coupling effects; hence, the coupling factor is less for structures with the larger density, As shown in the Figure 2.11 the variation is in the order of 0.498. Thus, it can be asserted that the coupling factor is proportional to the square root of the structural material density of the cylinder when coupled with water.

$$\text{Coupling Factor} \quad \propto \quad \sqrt{\rho} \tag{2.20}$$

However, at the far end of the geometric variation in the models of steel and copper, where the approximation fails, the variation of the coupling factor with respect to the structural material density is not as expected. Figure 2.11, and, 2.12 shows the variation of coupling factor for the thicker cylinder as of $r/t = 100$ with the fixed end boundary conditions. The variation is in the order of 0.46, for the thick cylinders of denser structures. This

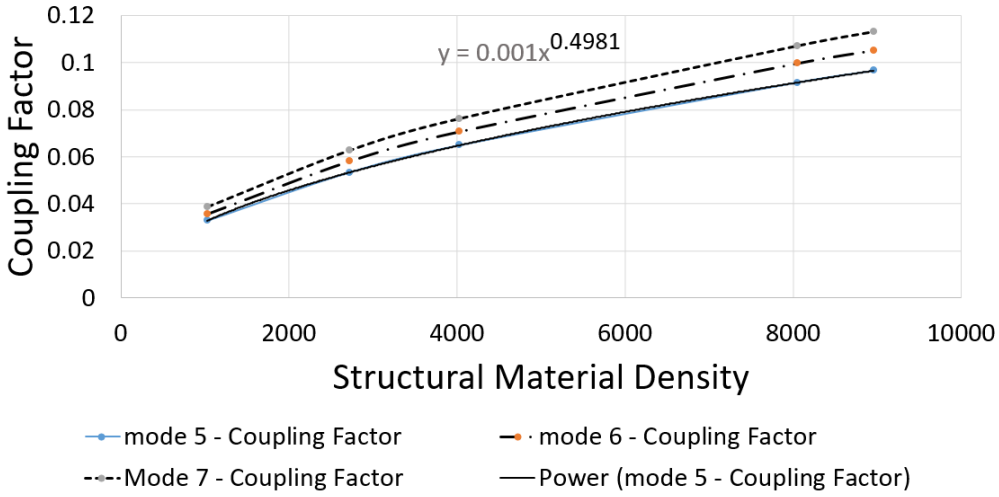

Figure 2.11: Effect of structural material density on coupling factor of water coupled cylinder with $r/t = 1000$

response is independent of the boundary conditions as both fixed end and cantilever end boundary conditions behaves in the similar way Figure 2.13 and 2.14. In the latter sections of this report, the conditions for each material, which this parametric study is limited to, are explained.

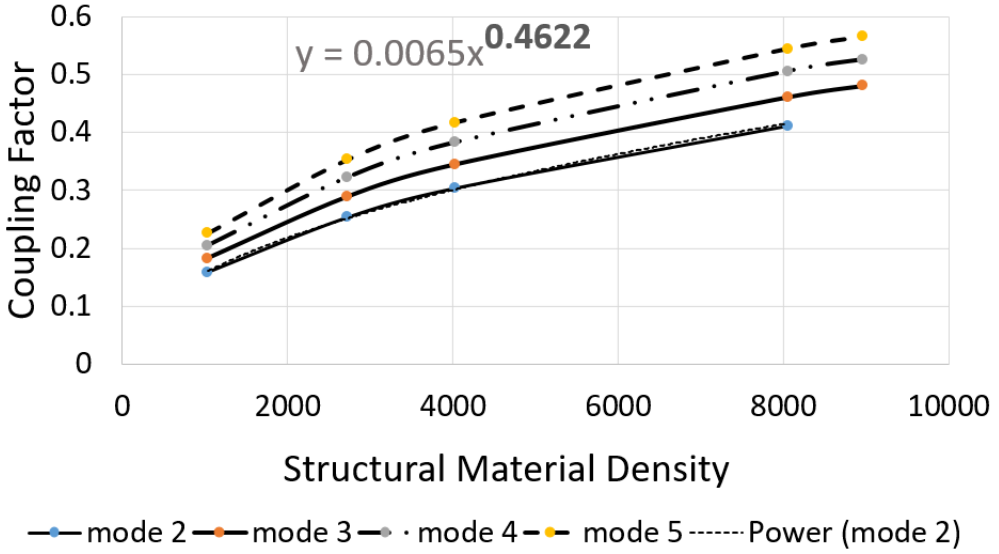

Figure 2.12: Effect of the structural material density on the coupling factor of a water coupled cylinder with $r/t = 100$

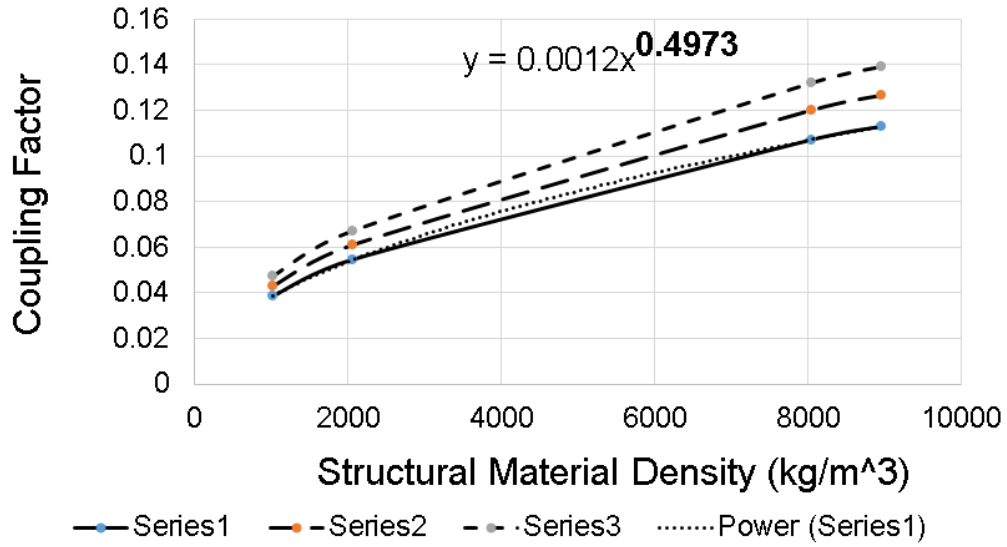

Figure 2.13: Effect of the structural material density on the coupling factor of a water coupled cylinder with $r/t = 2000$ - cantilever boundary condition

2.5.3 Effect of the longitudinal modes of cylinder on the coupling

Throughout this analysis importance is given only to the radial modes. The geometries of the cylinders are made so that longitudinal modes are avoided and first few natural modes for the convenience of the analysis. It is expected to find an interdependency between these modes, as by definition of these different natural modes they are orthogonal to each other. Thus, there is no interrelation of these modes with respect to coupling factor.

For clarification, the Table 2.6 compares the coupling factor of first longitudinal mode with higher longitudinal modes for the same radial mode number of the cylinders coupled with water. Similar analyses are done for numerous models to verify results. In all of these analyses, the effect of longitudinal modes of vibration on the coupling factor is found to be very minimal or negligible.

2.5.4 Relating the natural frequencies of the empty and water-coupled cylinder coupled

From the parametric study of all the factors mentioned above, the coupling factor which related the uncoupled system to the coupled system can be expressed as function of these

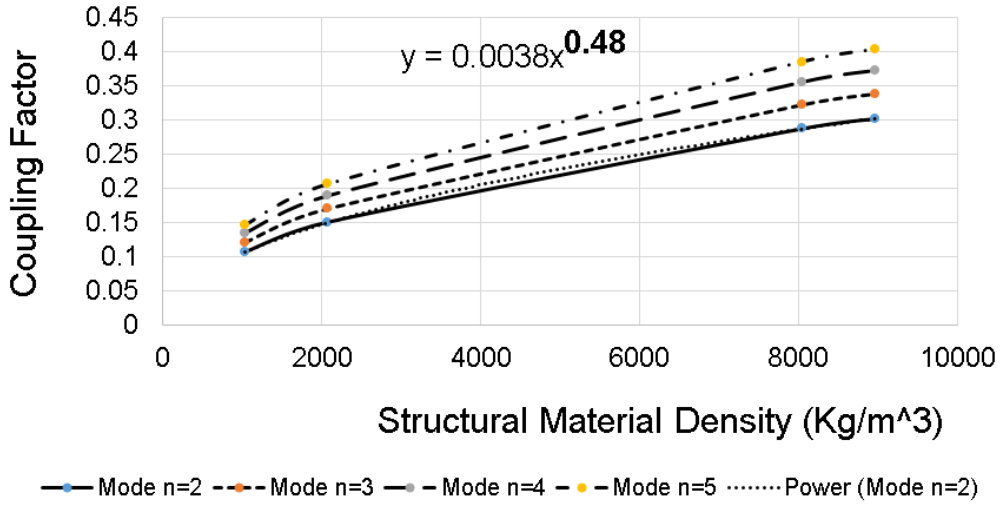

Figure 2.14: Effect of the structural material density on the coupling factor of a water coupled cylinder with $r/t = 250$ - cantilever boundary condition

Table 2.6: Coupling Factor for different longitudinal and radial modes

4^{th} Radial Mode		5^{th} Radial Mode		6^{th} Radial Mode	
Longitudinal Mode No.	Coupling Factor	Longitudinal Mode No.	Coupling Factor	Longitudinal Mode No.	Coupling Factor
1	0.170	1	0.186	1	0.203
2	0.170	2	0.187	2	0.203
3	0.171	3	0.188	3	0.204
		4	0.189	4	0.205

variables in their respective orders.

$$\begin{aligned} Coupling Factor &= \sqrt{\frac{\rho_s\ n\ t}{\rho_w\ r}} \\ \frac{Natural\ Frequency\ of\ Coupled}{Natural\ Frequency\ of\ Uncoupled} &= \sqrt{\frac{\rho_s\ n\ t}{\rho_w\ r}} \end{aligned} \tag{2.21}$$

where;

ρ_s = Density of the structural material.; ρ_w = Density of water.

r = Radius of the cylinder.; n = Radial modes of cylinder.

t = Thickness of the cylinder shell.

A wide range of structures and geometries of the cylinder holds good this expression with an error margin of less than 5 percent. Results of all the analyses are not illustrated, but to get the sense of breadth of the analysis, the results of the far end of the factors assessed are tabulated below. For metal cylinders such as steel and aluminum, whose stiffness and density is much higher than that of water, Tables 2.7 and 2.8 show the FEM and results from Equation 2.21 of the coupled and uncoupled modal frequencies. The expression will have the least error only for very thin shells of the cylinder, but for soft materials like ABS, the calculated results match closely even for thick cylinders as illustrated in Tables 2.9 and 2.10.

Table 2.7: Approximated modal frequency of the coupled cylinder-1

Steel Cylinder with $r/t = 10000$ coupled with Water				
Radial Mode No.	Modal Frequency (Hz)			Error Percentage
	FEM Results		Approximated Results	
	Empty Cylinder	Coupled Cylinder	Coupled Cylinder	
9	8.901	0.769	0.757	1.47
10	7.481	0.680	0.671	1.36
11	6.568	0.628	0.618	1.55
12	6.062	0.604	0.595	1.47
13	5.893	0.613	0.602	1.8

Table 2.8: Approximated modal frequency of the coupled cylinder-2

Steel Cylinder with $r/t = 100$ coupled with Water				
Radial Mode No.	Modal Frequency (Hz)			Error Percentage
	FEM Results		Approximated Results	
	Empty Cylinder	Coupled Cylinder	Coupled Cylinder	
2	72.448	29.839	29.070	2.578
3	52.074	24.045	25.590	6.42
4	74.734	40.847	42.407	3.8
5	116.361	65.427	73.822	12.8
6	169.453	107.964	117.765	9.07

Table 2.9: Approximated modal frequency of the coupled cylinder-3

ABS Cylinder with $r/t = 200$ coupled with Water				
Radial Mode No.	Modal Frequency (Hz)			Error Percentage
	FEM Results		Approximated Results	
	Empty Cylinder	Coupled Cylinder	Coupled Cylinder	
3	23.22	3.03	2.88	4.9
4	18.53	2.72	2.66	2.4
5	22.49	3.65	3.60	1.23
6	30.90	5.45	5.43	0.48
7	41.83	7.94	7.94	0.01

Table 2.10: Approximated modal frequency of the coupled cylinder-4

ABS Cylinder with $r/t = 20$ coupled with Water				
Radial Mode No.	Modal Frequency (Hz)			Error Percentage
	FEM Results		Approximated Results	
	Empty Cylinder	Coupled Cylinder	Coupled Cylinder	
2	167.98	57.64	53.91	6.46
3	166.31	64.31	65.37	1.64
4	267.11	114.01	121.23	6.33

As other factors are analyzed independently, the variation in errors in these calculations is related significantly to the radial mode number. It is challenging to track the nonlinear or higher order relations of radial modal frequency with coupling by a parametric study. Thus, the analysis is further constrained to a set of models for every structural material of the cylinder.

Commenting on the results, it is a well-known fact that in a lower order natural frequency, fluids might act as added mass, which in turn implies that the densities of the fluid and structure dictates the coupling provided that the structure is thin enough compared to its elasticity to lower the effect of the structure's stiffness, so the error in the expression increases for thicker and smaller cylinders. It is obvious that the stiffness and the phase velocity of the structure and fluid play a very important roles in the coupling. As these

are not considered explicitly in the expression, the effect of those parameters will eventually take precedence as the shells get thicker. This is also the reason for which Equation 2.21 is restricted to water. The conditions where the Equation 2.21 is valid for the approximation are listed below for Steel (High density) and ABS (Low density - polymer);

$$Steel : 100 \leq r/t$$

$$ABS : 20 \leq r/t$$

For the cylinders lower than the stated radius to thickness ratio, the error in the approximation is no longer negligible. The stiffness of the structure and thus the phase velocity need to be analyzed theoretically with higher order equations to get the relation with the coupling factor, which is outside of the scope of this parametric study.

2.6 Conclusion

The importance of the coupling factor in the modal analysis of the fluid-coupled structures is shown through this study and realized by the proposed expression Equation 2.21. Proposed also is an apparent transition condition (see Figure 2.22) to differentiate strong and weak coupling of the cylinder's structure with fluids. Care should be taken when designing the cylinders and encountering dense fluids such that the geometry can avoid the strong coupling with the fluid. The flexural wave speed in the structure is reduced due to the interaction with the dense fluid when compared to a given mode of vibration in a vacuum (see Equation 1.3). Hence, coupled structures achieve their first few natural modes at a lower frequency, and this theory is widely studied and accepted. Thus, the results obtained are convincing based on this theory. For the explanation that the variation of coupled natural frequency is much less dependent on the material stiffness (modulus of elasticity) of the structure, it is noteworthy that the equation (Eq.2.21) is similar to the one discussed in "Vibration of a Cylindrical Shell in an Acoustic Medium" by G. B. Warburton [59], which is also independent of the elasticity modulus, except for the displacement component factor.

However, we cannot move forward with that equation as it is more generalized and its equation is derived for infinite shell. For a specific finite cylinder, it is equally as complicated as of other theories with factors to be calculated based on the boundary conditions and displacement components. While Equation 2.21 is more specific and simple. The Equation 2.21 is an approximation to facilitate the design in terms of selecting the appropriate materials for the required geometry or vise verse, irrespective of the boundary conditions. Equation 2.21 can be generalized for a wide variety of structures and fluids with, acceptable error ranges from 1% to 10%.

$$\sqrt{\frac{\rho_s}{\rho_f}} \leq \sqrt{\frac{Radius}{Thickness\ of\ the\ shell}} \tag{2.22}$$

Rather than solving a 6^{th} or higher order differential equation or using the software, which also takes significant computational time, a simple equation for a specific system is more convenient from an engineering perspective. If the problems of fluid dynamics are not of primary interest, which is the case for most of the engineering systems, the efficient way is to deal with these approximations of a given system if the degree of error is not significant. This objective is served by Equation 2.21 for cylinders filled with water. Equation 2.22 can be regarded as the apparent transition condition to differentiate strong and weak coupling of the cylinder structure with fluids. Hence, this report will serve as a guide to further parametric analysis on coupling in similar systems and to gain insight into the coupling factor as well as where and how to start the study. These formulations find applicability in designing thin structures containing dense fluid(water). In the design of the membrane tubes used in medical equipment and the design of large cylindrical structures where the aspect ratio of the cylinder's diameter to thickness is close to the sated limit, this study will help in an evaluation of their modal characteristics.

Chapter 3

Simulation of the dynamic events of impact using an explicit 3D FEM model and validation through experimentation and contact models

In this study [39], a dynamic 3D model of a rod with a spherical-end impacting with a fixed flat surface is modeled using an explicit dynamics module under ANSYS Workbench. The model, as shown in Figure 3.1, is meshed with 3D elements with a Lagrangian reference frame. Considering the computational time, many simulations with different meshes are produced to have consistent results independent of mesh density. The maximum displacement over time of the base under impact for various mesh sizes is shown in Figure3.3. The x-coordinate represents the distance from the point of impact to the end of contact during the impact, and the y-coordinate represents the maximum deformation caused by the impact over time. As shown in Figure 3.3, it is evident that the maximum displacement response at the contact point is almost convergent for a mesh size of 0.002mm. It should be noted that in this convergence study, the path result of the displacement over the length of the contact accounts for discontinuity errors due to lack of sufficient nodes at the contact region. The mesh convergence is achieved with an element size of 10^{-5}, as shown in Figure 3.2, within 0.1mm around the vicinity of the impact point for both normal and oblique impacts. For the dynamic impact analysis, the time step of the simulation depends on the smallest element and sound wave speed in the material under test. As the event of the impact is in the order of milliseconds a time step of $2 * 10^{-9}$s is used in the simulation. To accommodate the whole event of the impact and sufficient time to plot the rebound velocity, the event is simulated for 10 microseconds. The models with different radii and lengths and impact velocities are meshed with 20 to 25 thousand nodes and 100 to 150 thousand elements based on the parameters of the rod. The rod is modeled in such a way that it is 0.001mm away from the base

so that computational time can be saved in the dynamic analysis. AUTODYNA solver is used for the analysis. Normally in the dynamics simulation, mass scaling is used to improve the time efficiency of the computation. Mass scaling is the process where the density of the material is artificially increased for the smallest element by which the larger time step can be used to save on time taken to solve the simulation. But in this impact analysis, as the smallest element of the structure is at the point of impact, change in the density of the elements results in change in inertial aspects of the impact. Hence, in an explicit dynamics simulation of impact, we cannot have the luxury of mass scaling to reduce the computation time. The computation time is between 6-7hrs on a computer with an i7 processor with 16GB RAM. More than 200 different cases of simulations are performed. Results are analyzed and correlated with the mentioned prominent models of impact mechanics and experimental results. The time step for all the dynamic analyses is in the order of 10^{-8}s as the event of impact is in the order of 10^{-5}s. The range of material and geometric parameters modeled in these simulations are in exact co-rrelation with those used in the experiments and in the mentioned contact models.

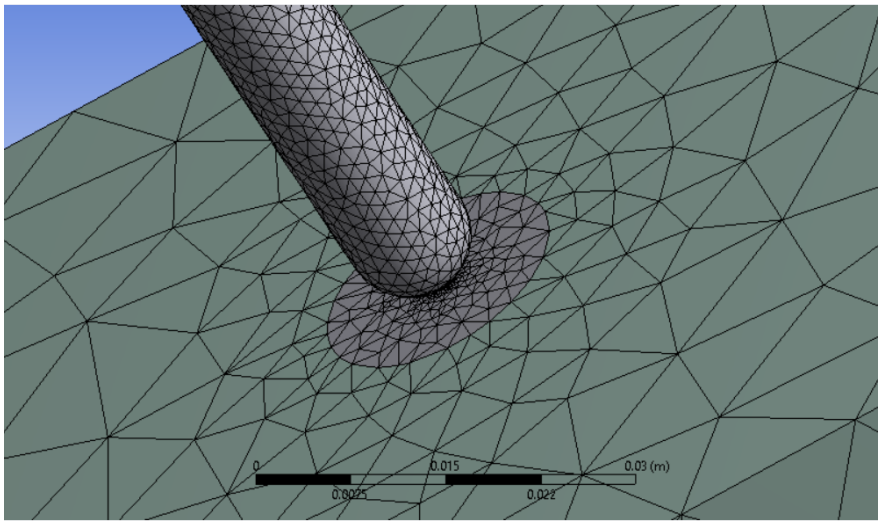

Figure 3.1: FEM model of the impact of a rod on a flat surface

In the explicit dynamics, for the simulation of impulsive loading as in the case of impact or detonation, the material behavior in the plasticity zone is affected by the type of loading,

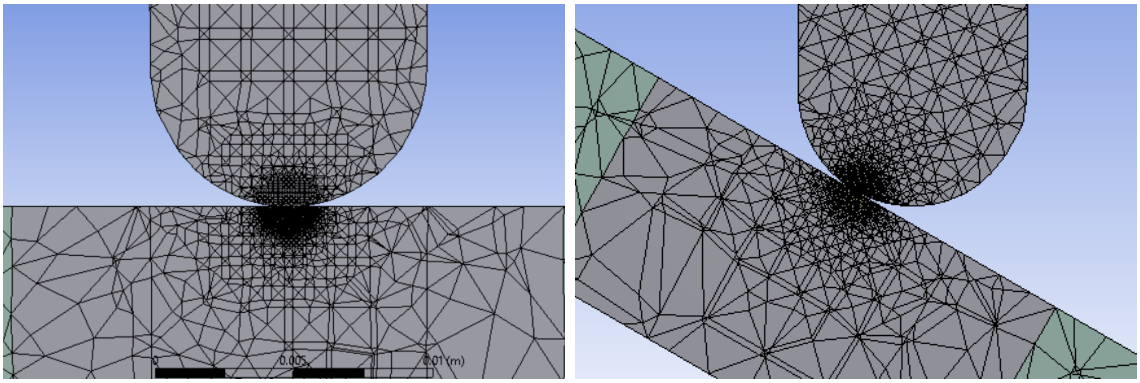

Figure 3.2: Cross-sectional view of the mesh for normal and oblique impacts of the rod

strain rate, and temperature. For the computation of these systems, along with the elastic properties of the material, plastic and failure properties of the materials are defined by many formulations. Each formulation of the material's hardening properties by these models addresses the change in properties of the material at the specific scenario. Formulations used in the ANSYS Workbench to define the plastic properties of the materials are briefly described here.

Bi-linear, multi-linear, and nonlinear isotropic hardening is when, after an initial yielding point, the stress as a function of plastic strain can be expressed as a linear slope (tangent modulus), as a set of experimental values of stress for a respective plastic strain or as an exponent of strain (power law). These hardening laws are generalized plasticity formulations which do not account for change in the material behavior for strain rates or impulsive loads. These properties can be used if there are experimental values of stress strain plots for the given strain rate.

One of the popular plasticity studies for the computation of high velocity impact and stress flow in the materials for the thermal loads is Johnson-cook strength model. This constitutive model is used for computation of flow stress accounting the effects of strain hardening, strain hardening rate and thermal softening.

Cowper Symonds's and Zerilli Armstrong's strength models in principle follow the Johnson-Cook model with the different modifications. The Cowper Symonds strength model

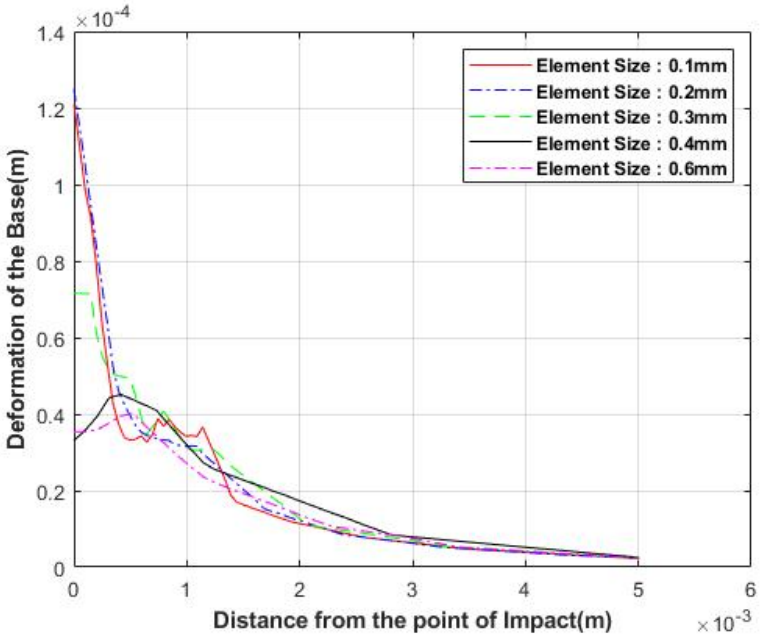

Figure 3.3: Maximum base deformation over the contact region for different mesh densities

is normally used in the simulation of metal cutting, which dictates the formation of the chips and hardening of the material in the process. According to Zerilli and Armstrong, materials have their own constitutive behaviors based on their molecular structure type, as in body-centered or face-centered, which have distinctive dislocation characteristics.

Another popular study of plasticity is the Steinberg Guinan strength model used to model the shock wave in the metals as a result of a very high velocity impact. In this elastic-plastic constitutive model, the dependency of shear modulus of the metal on the rate of change in pressure and temperature is addressed.

For our study, the material property was defined using all of these models and simulated low velocity impact which is our point of interest. For the bilinear, non-linear or power law hardening models, the results of the deformation and rebound velocity are not consistent with the other contact models and experimental results. The material property given in these models is not accurate and will not account for the strain rate. The Cowper Symonds Strength and Zerili Armstrong strength model parameters were not experimentally calculated, and approximated values of those parameters did not provide comprehensive results.

These studies were not formulated to account for impact analysis. Although the Steinberg Guinan's strength model is formulated to facilitate the computation of impact analysis, this model in particular deviates from the experimental results for low velocity impacts. Thus, for our study, the Johnson-Cook strength model is used to define the elastic-plastic properties of the metals we are testing for impact behavior.

Johnson − Cook Strength

The Johnson-Cook strength parameters are used in this low velocity impact study to account for plasticity in the material. In this model the flow stress is expressed as follows:

$$\sigma = \underbrace{(A + B\epsilon^n)}_{\text{strain hardening}} \quad \underbrace{(1 + C\, ln(\epsilon^*))}_{\text{strain rate strengthening}} \quad \underbrace{(1 - T^m)}_{\text{temperature}} \tag{3.1}$$

where;

σ = Equivalent stress; A = Initial yield stress;

B = Hardening constant; ϵ = Plastic strain;

n = Strain hardening exponent; C = Strengthening coefficient of strain rate;

ϵ^* = Normalized effective plastic strain; m = Thermal softening coefficient

These parameters can be obtained by true stress strain plot [10] [21] of the materials at different strain rates. Table 3.1 lists the material properties of the rods and bases used in this study based on the Johnson-Cook-strength model.

3.1 Experimentation and motion analysis

The experimental setup is shown in Figure 3.4. The impacting base is fixed on a rigid table. A robotic arm is used to drop the rod vertically from different heights. Two lights,

Properties	Rod (AISI 201)	Flat (AISI 1010)
ρ	7800 (kg/m^3)	7830 (kg/m^3)
E	212 (GPa)	200 (GPa)
ν	0.28	0.28
A	750 (MPa)	300 (MPa)
B	1793 (MPa)	633 (MPa)
n	0.523	0.13
C	0.014	0.014

Table 3.1: Material properties of the rod and base

1000W each, have been used to capture a clear image during the impact. A high-speed camera capable of recording $10,000$ frames per second (fps) is used to capture the motion of the rod before, during, and after the impact. After each impact, the event of the impact is recorded and measured. 10 clear trials of each rod impact have been recorded and analyzed with motion analysis to ensure consistent results. Using this setup, both normal and oblique impact analyse are done. The whole event of the impact is captured and recorded by the high-speed camera.

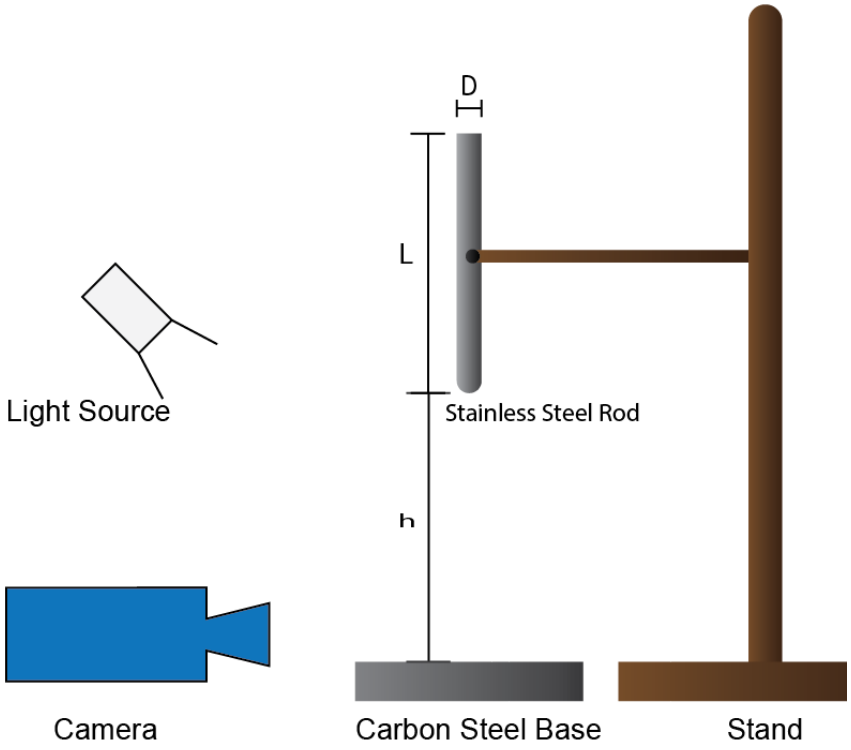

Figure 3.4: Schematic representation of the experimental setup

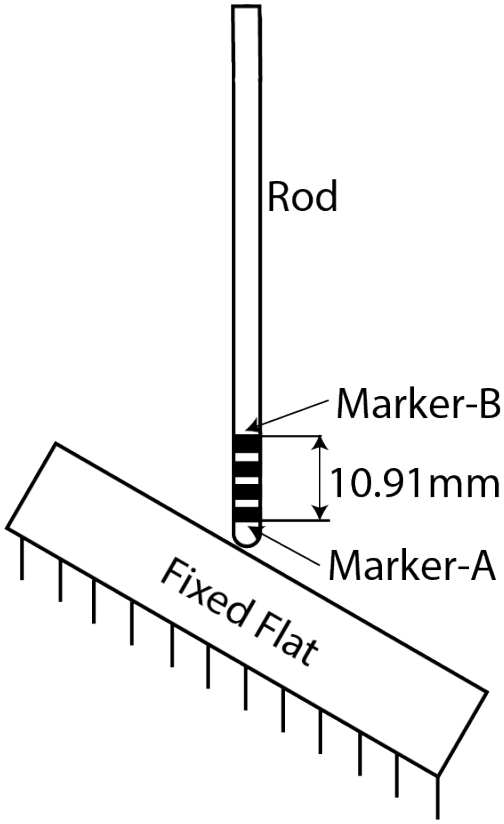

Figure 3.5: Oblique impact of rod-2

Each recorded clip is trimmed to get at least 300 frames close to the point of the impact of the rod, and each frame contains 512*512 pixels. A Motion analysis software is used to calibrate and measure the position of the rod over time. To calculate the velocity of the rod before and after the impact, a certain point on the rod has been tracked. Figure 3.6 shows the normal impact of a rod and the tracking of a point. The red dot indicates the tracker marks as the rod moves.

The motion of the rod before impact and after the impact has been accurately captured. These motion frames are calibrated to get an actual displacement profile of the impact over time. The displacement plot of the contact point is used to calculate the velocity of the rod, as shown in Figure 3.7. The velocities have been calculated from the slopes of the displacement plot before and after the impact, respectively.

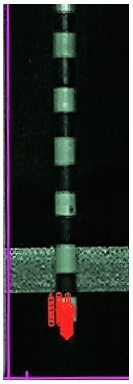

Figure 3.6: Tracking the normal impact of rod-2

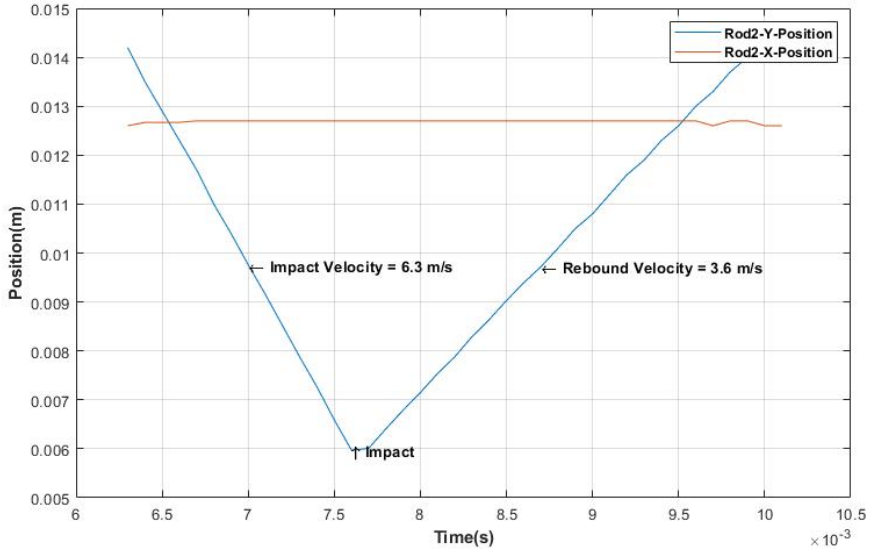

Figure 3.7: Displacement plot of the tip of rod-2

3.2 Results and comparison

3.2.1 Comparison of the coefficients of restitution

The first step in the process of validation of the FEM simulation is done by comparing the simulation and experimental results of the coefficient of restitution for 3 different rods dropped from the same height of 0.8m. The properties of the rod and base are described in the section on the plasticity models in Table 3.1. Table 3.2 shows the dimensions of the rods subjected to the impact study. Table 3.3 is the comparison of experimental results to simulation results of the COR of the rod. In the simulation of the impact, the direct results

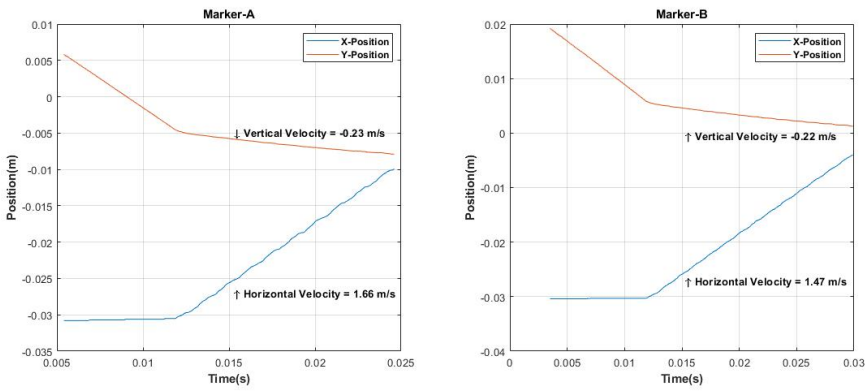

Figure 3.8: Displacement plot of 2 markers on rod-2 impacting at 30 degrees

of the velocity of the rod after the impact are subjected to substantial variation because of the vibration and shock waves in the rod. The velocity measured at each node at a given time is different across the length of the rod. Even the average nodal velocity of the whole rod has quite a significant deviation between the maximum and minimum value of the velocity at any given time. To minimize this deviation, the velocity is measured as slope of the deformation of the whole rod. Thus, this deviation of velocity is averaged over the time after the contact rather than instant velocity given by the velocity probe. From these results, it is evident that, for the same impact velocity irrespective of rod dimensions, the simulation results are in correlation with experimental results. The experimental results of the COR are lower than the simulation results by less than 10 percent. This can be explained as a factor of surface roughness and friction during the impact, which is not accounted for in the FEM simulation. Comparing the results of COR with the experiment validates the basic mesh convergence and the basic energy balance between the contact bodies. To further validate the results, a similar study was done with oblique impact of the rod. Rod-2, as mentioned in the Table 3.2, was subjected to oblique impact with a different angle, and the same system is modeled and simulated. Figure 3.8 shows the displacement plot of 2 different points on rod-2 impacting at an angle of 30 degrees to the base. These tacking points are denoted as marker A and marker B in Figure 3.8; V_A and V_B are the resultant radial velocity of the points respectively. Angular velocity ω of the rod is calculated by Equation 3.2. Table 3.4 depicts

	Diameter(m)	Length(m)
Rod-1	0.0096	0.190
Rod-2	0.00640	0.19
Rod-3	0.00475	0.2

Table 3.2: Dimensions of the rods used in the study

Rod	COR	
	Experiment	FEM
1	0.406 $\pm$0.012	0.463
2	0.420$\pm$0.005	0.485
3	0.559$\pm$0.008	0.602

Table 3.3: COR of the rod undergoing normal impact

the comparison of angular velocity of the rod between the experiment and simulation for different angles of impact. In both the experimental results and explicit dynamic simulation results, the COR is subjected to variations and therefore cannot be the primary method to validate or to analysis the impact behavior. Further validation is needed for the simulation with respect to the deformation of the base and the rod during the impact.

$$\omega = \frac{V_A - V_B}{Distance\ between\ marker\ A\ and\ B} \tag{3.2}$$

3.2.2 Comparison of the permanent deformations of the base

In the next step, a prominent study in the impact of the rod is taken as a reference to obtain experimental data of the rod impacting a base, and the same model was simulated. The experimental results are taken from a reference paper[17], which is a study done by one of the present authors of this paper. In this paper, a rod of stainless steel (AISI 201) and

Angle of impact	Angular Velocity (rad/sec)	
	Experimental	Simulated
45°	21.5$\pm$0.002	22.07
30°	16.8$\pm$0.004	16.73
15°	9.6$\pm$0.005	10.12

Table 3.4: Experimental and simulation results of the angular velocity after impact

base of Carbon steel (AISI 1070), whose material properties are the same as described in our study, are tested for impact over different drop heights. The permanent deformation and kinematic coefficient of restitution is measured using a similar motion analysis. The same research is extended in this study to validate our 3D explicit dynamics simulation with these experiments.

Figure 3.9 compares the experimental data and simulation results of permanent deformation of the base when a rod of 300mm length and 9mm diameter with a spherical end impacts a surface with different drop heights. The results of he permanent deformation of the simulation correlates well with the experimental and contact model results.

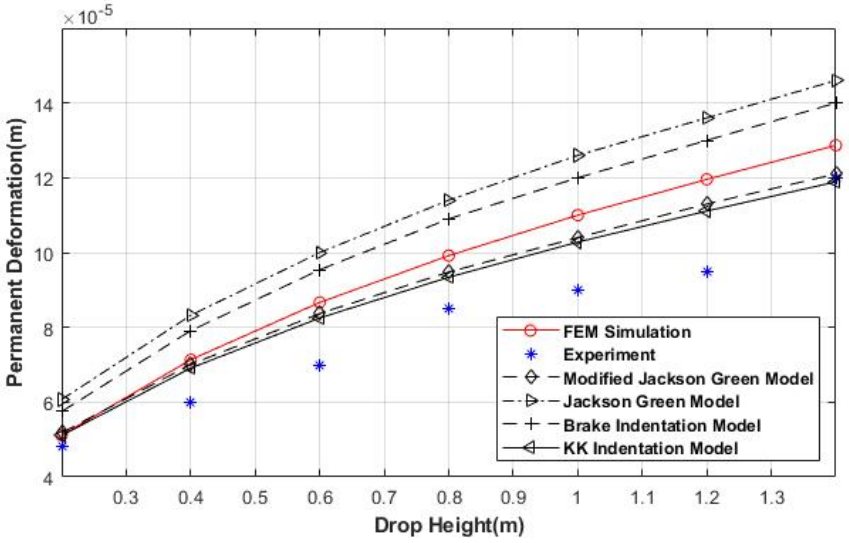

Figure 3.9: Comparative simulation results of permanent deformation of the rod with reference paper results

From the graph, it is evident that the results of the simulation are in correlation with the experiment and contact models. From the graph, it is also evident that the permanent deformation of the base is in correlation with the contact model; especially with the modified Jackson Green model, the results are closer to the experimental results. The presented dynamic simulation method accounts for deformation on both bodies undergoing impact, which is the main principle on which the modified Jackson Green model was formulated; hence the correlation is justified. Figure 3.10 shows the reaction force with respect to the

deformation of the base for different drop heights of impact. Reaction force F^r can be calculated from the nodes where boundary conditions are defined. It is the response of the structure for all the loads acting on it. In a basic sense, reaction force is the difference between the summation of elastic static (${F_e}^k$), damping (${F_e}^c$) and inertial (${F_e}^m$) loads to the applied loads (F^{nd}) as shown in the Equation 3.3.

$$F^r = -\sum_{e=1}^{N}[{F_e}^k + {F_e}^c + {F_e}^m] - F^{nd} \tag{3.3}$$

Close observation of this graph shows that, for the linear progression of impact velocity, the deformation tends to reduce with the effect of higher strain hardening under higher strain as the impact velocity increases.

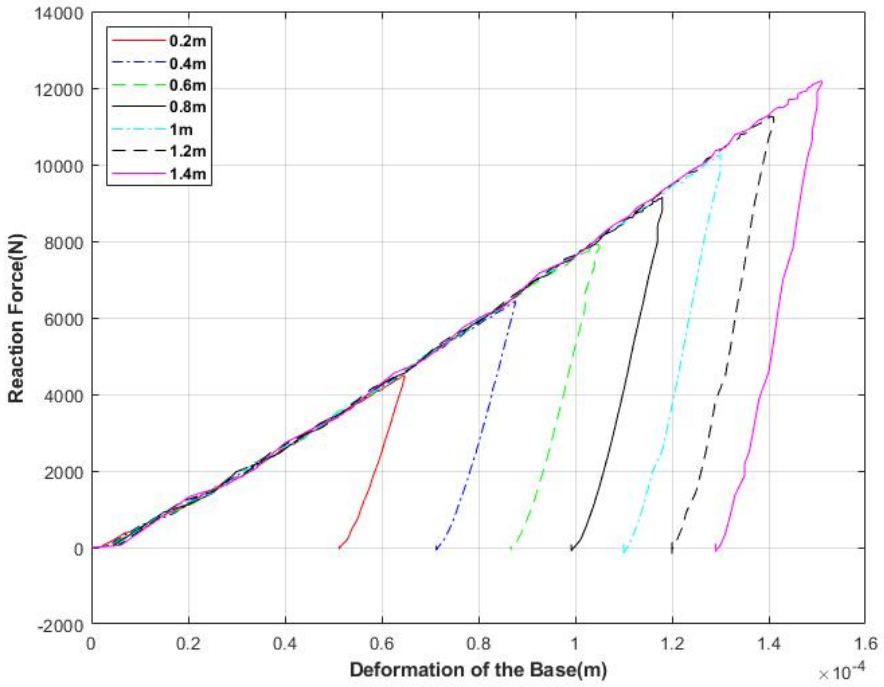

Figure 3.10: Force reaction vs deformation of the base for different impact drop heights

3.2.3 Permanent deformation of the rod

An attempt is made to determine the permanent deformation on the rod, which is not directly available in the analysis solution. ANSYS simulation measures the deformation as the change in the position of the node during the simulation. But when a body without a boundary condition or constraint undergoes a displacement, that is considered the deformation in the simulation results. In our case of impact analysis, the rod undergoes both free-body motion and deformation during the impact. One convenient way to separate the factor of free body motion from the deformation plot is to find the difference in the displacement of the rod at any point on the rod from the impact point. But the resulting deformation of the rod will be inconsistent, as the rod undergoing the impact will have compression and vibrations along the process of impact. This problem can be solved by measuring the plastic strain on the nodes near the point of impact as shown in Figure 3.11. Deformation of the rod is obtained by measuring the difference in the displacement of the node at the point of impact to the nearest node to it and then to the impact point at which the plastic strain is 0.

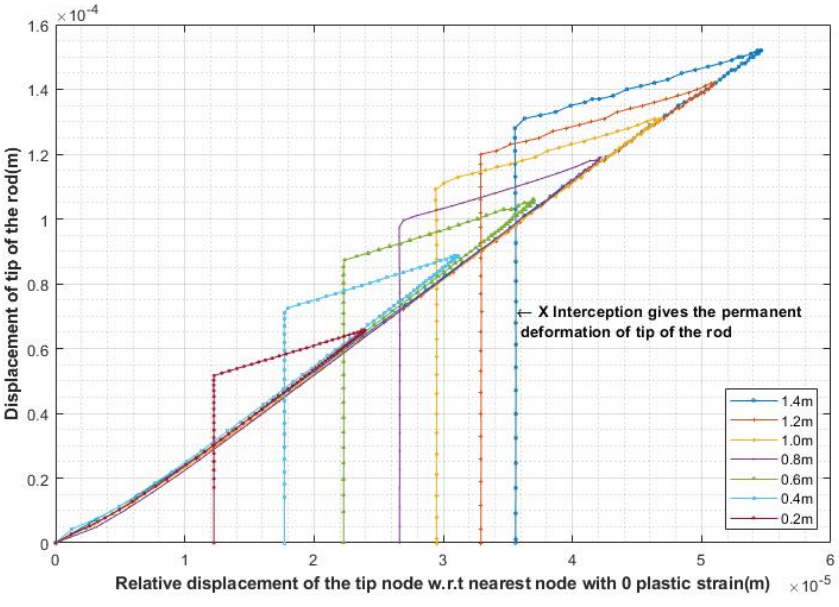

Figure 3.11: Measuring the permanent deformation of the rod by the relative displacement of the rod tip

The plot of this displacement also shows the impact phases of compression and restitution. After the contact ends the plot is parallel to the y-axis, thus representing no relative displacement between the nodes; that should be the permanent deformation on the rod which cannot be recovered. Figure 3.12 depicts the permanent deformation of the rods for different drop heights.

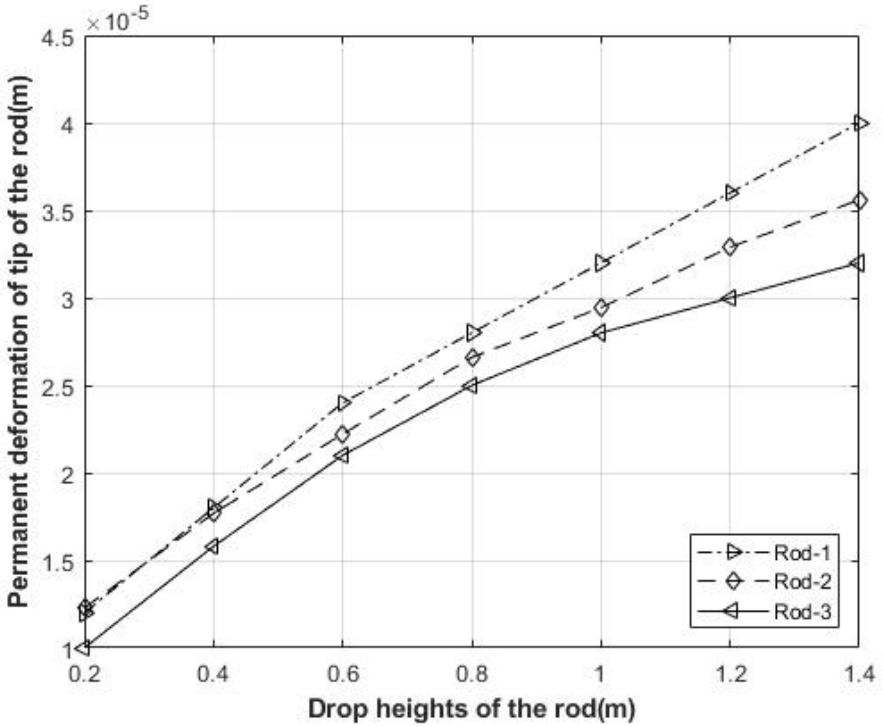

Figure 3.12: Permanent deformation of the rod for different impact drop heights

3.3 Stress waves in the rod

In the dynamic simulation, the event of impact will generate a stress wave in the rod. For the free-boundary condition, the stress wave should correspond to the speed of sound in the material. In order to validate this dynamic aspect of the system, hoop strains over the length of the rod are measured. The times at which the strain is at its maximum at different specified points in the rod are noted. Figure 3.13 represents this maximum time relative to the respective points over the length of the rod. The slope of this graph provides

the stress wave speed in the rod. From this graph, it is evident that the dynamic behavior of the simulation is valid for this analysis.

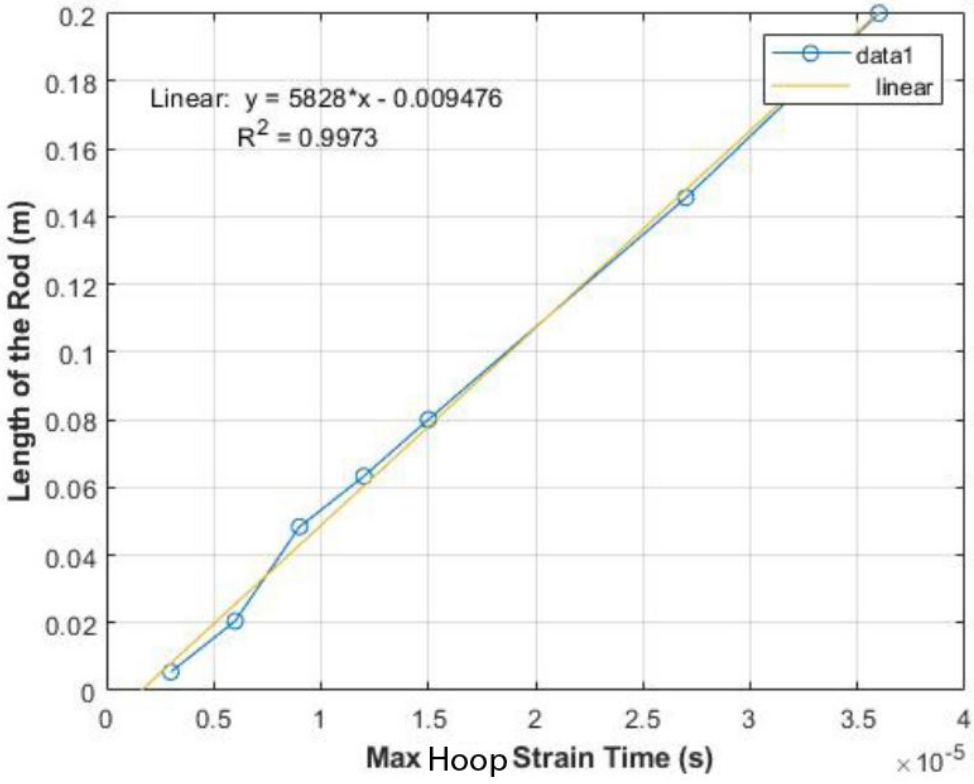

Figure 3.13: Stress wave speed in the rod after impact

3.4 Conclusion

In this study, impact models are simulated using 3D modeling and the dynamic event of the impact is analyzed using an explicit dynamic solver. This method of 3D dynamic simulation has been validated by experiment and contact models. The first step in the validation is the comparison of experimental results on COR of normal impact and the angular velocity of the oblique impact. In the second step, from the correlation between the simulation and a reference study[19] of impact of the rod on permanent deformations of the base, it is evident that the result presented in the reference study further validates the presented simulation on analysis of deformation during and after the event of impact. This same model is also compared with the prominent indentation and flattening contact models. From that comparison, it evident that the simulation results are in close agreement to the modified Jackson Green model, as the principle under the modified Jackson Green model study also considers deformation on both bodies undergoing impact. Furthermore, the effect of the strain rate is shown by the progression of permanent deformation with the impact velocity. With these comparisons, it can be inferred that the 3D explicit dynamics analysis presented in this study is valid for the impact analysis of the spherical end on a flat surface; hence, the same technique can be used to study more complicated models without necessitating re-validating the system. A method to determine the deformation of a rod undergoing impact is presented. This study can be further extended to validate the deformation of the rod with the experimental results. The presented modeling and simulation technique can serve as guide in the design of robotic arms where these low velocity impacts are more prevalent. Given that there are no predefined conditions in the proposed simulation method of impact, this technique can be used to simulate and study the low velocity impact behavior of composite structures.

Chapter 4

Effect of fluid structure interaction during the impact

This chapter provides an extension to a previous study. In the Chapter 2, we showed that the natural frequency of fluid-coupled cylinders can be approximated by the uncoupled natural frequency of the cylinder. We modeled and validated the dynamic event of the impact of rods. Following these chapters, an attempt is made to study the behavior of the cylinders during the event of impact under the influence of fluids. The effect of fluid being in the tube on deformation and the coefficient of restitution after the impact is studied. Insight regarding how contact force, energy, and stress distribution are affected by fluid during the event of impact is presented. The influence and importance of the natural frequency of the coupled tube on the duration and resulting multiple impacts during the restitution phase for the oblique impact is presented.

4.1 Modeling and simulation of the impact of water-filled tubes

Similar techniques to those used in Chapter 3 are used to model the water-filled tubes impacting on the flat base. In particular, two different models are developed for this system; the Lagrangian and Eulerian methods are used to represent water elements. In a Lagrangian reference frame, each element of the mesh is used to represent the volume of a material. The same amount of material mass remains associated with each element throughout the simulation. The mesh deforms with the material deformation. Solving using a Lagrangian reference frame is the more efficient and accurate method to use for the majority of structural models. In a Eulerian reference frame, however, the grid remains stationary throughout the simulation. Material flows through the mesh. The mesh does not therefore suffer from distortion problems, and large deformations of the material can be represented. Several simulations

were performed in a preliminary phase using both methods to achieve mesh convergence with both models.

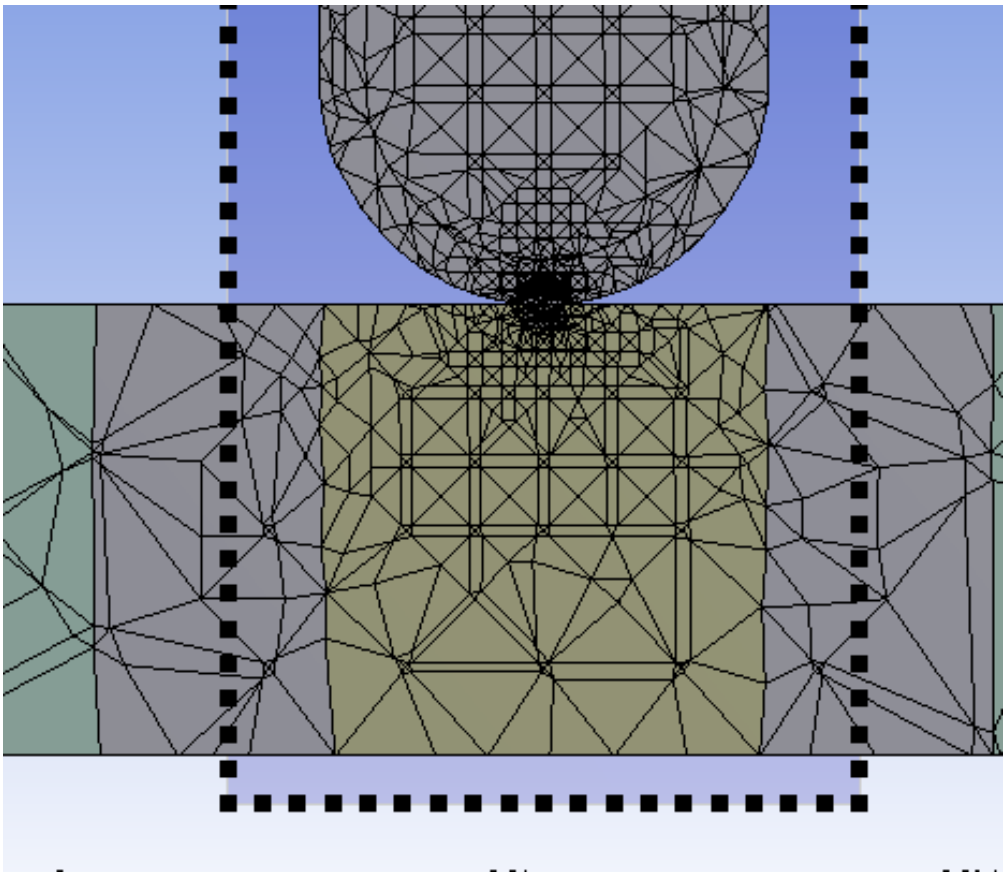

Figure 4.1: Meshing in a Eulerian Reference Frame

Figure 4.1 represents the meshing in a Eulerian reference frame. For our study, the simulations results using both methods show corelation. However, simulation using a Eulerian reference frame is computationally very expensive compared to using a Lagrangian reference frame. The additional computational cost comes from the need to transport material from one cell to the next and also to track in which cells each material exists as void and is also considered as a material in this sense. The present study is focused on the event of impact, which is of a minute time scale in the order of micro to milliseconds, and fluid flow is not involved in our analysis. Hence, all further simulations in our study are done using a Lagrangian reference frame. To analyze the effect of impact behavior of the fluid-filled tube, each impact parameter is studied further using these simulation results.

4.2 The COR of the tube under the influence of fluid

The coefficient of restitution can describe changes in energy and velocity before and after a collision concisely. Figure 4.2 represents the COR of the tube of length 0.01m with a 0.01m diameter with different thicknesses impacting on a flexible base. The ratio of thickness to the diameter of the tube has a significant effect on the rebound velocity of the tube filled with water.

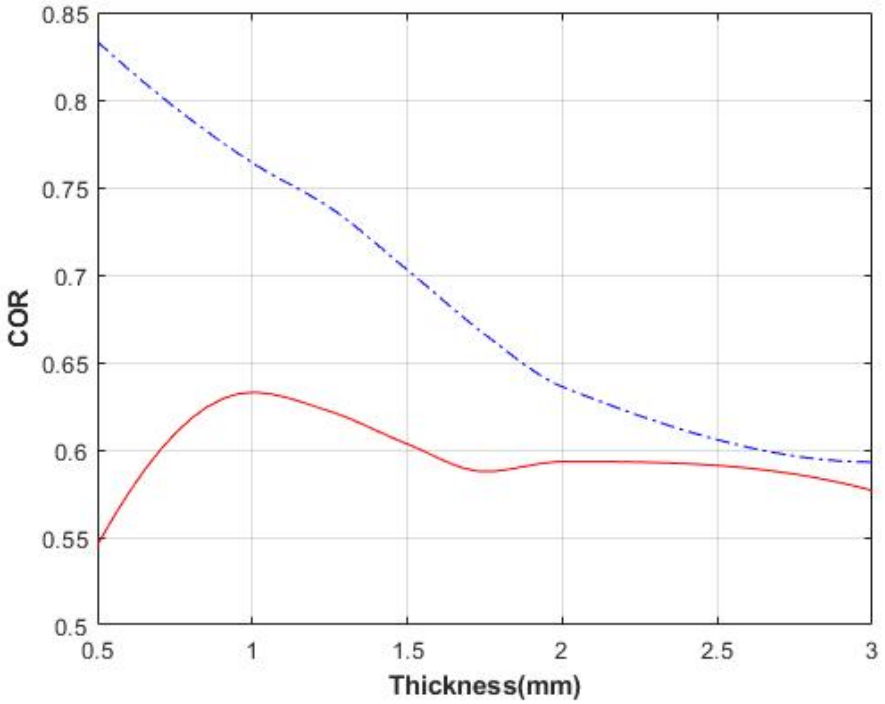

Figure 4.2: COR of tube with the impact velocity of 1m/s

This behavior is similar to the modal frequency of the coupled cylinders. As the graph represents for the thick-walled tube, the COR is not affected by the presence of fluid inside it. The CORs of fluid-filled and empty tubes deviate from each other as the thickness of the rod is reduced. However, after a certain lower limit of thickness, the COR takes a drastic deviation between the COR of empty and fluid filled tubes. This limit on thickness of the tube matches the strong coupling condition Equation 2.22 proposed in Chapter 2. The rebound

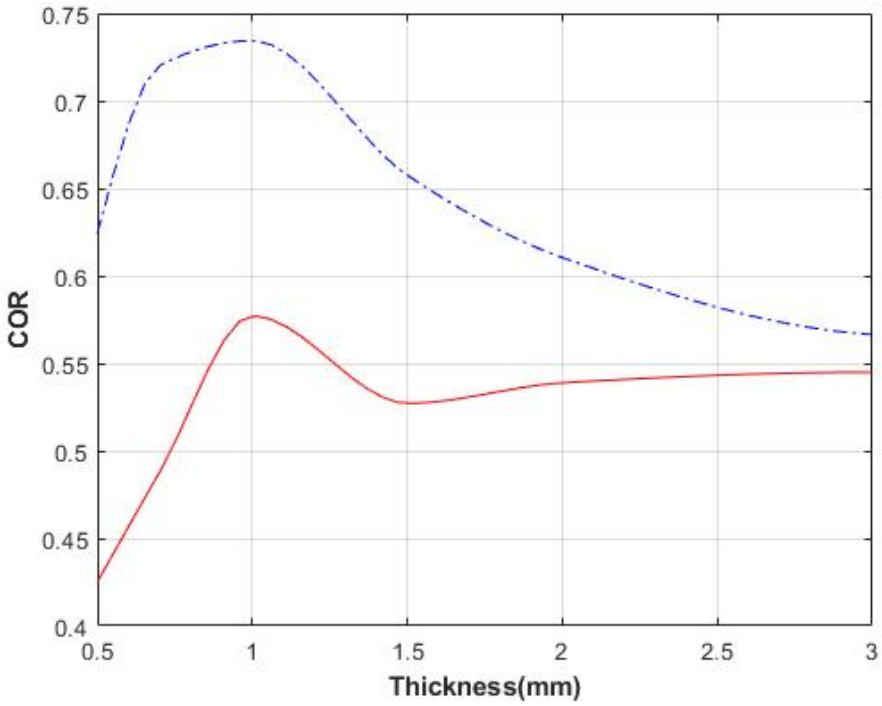

Figure 4.3: COR of a tube with the impact velocity of 2m/s

velocity of the fluid-filled tube is significantly reduced once the aspect ratio of thickness to diameter of the tube is below the stated limit.

Figures 4.6 and 4.7 show that this pattern of results is consistent for different diameters of the tube and different impact velocities. The resulting variations in the COR of the fluid-filled tubes can be attributed to contact force, plastic deformation, and energy transfer between the fluid and the tube.

4.3 The contact force during the event of the impact

In finite element analysis, the contact between the two bodies is enforced based on three conditions: 1) No penetration between the bodies 2) Balance between the applied and the contact forces in case of static problems. 3) Conservation of momentum in case of dynamic problem as in the case of impact. In general, there are two popular formulations that meets

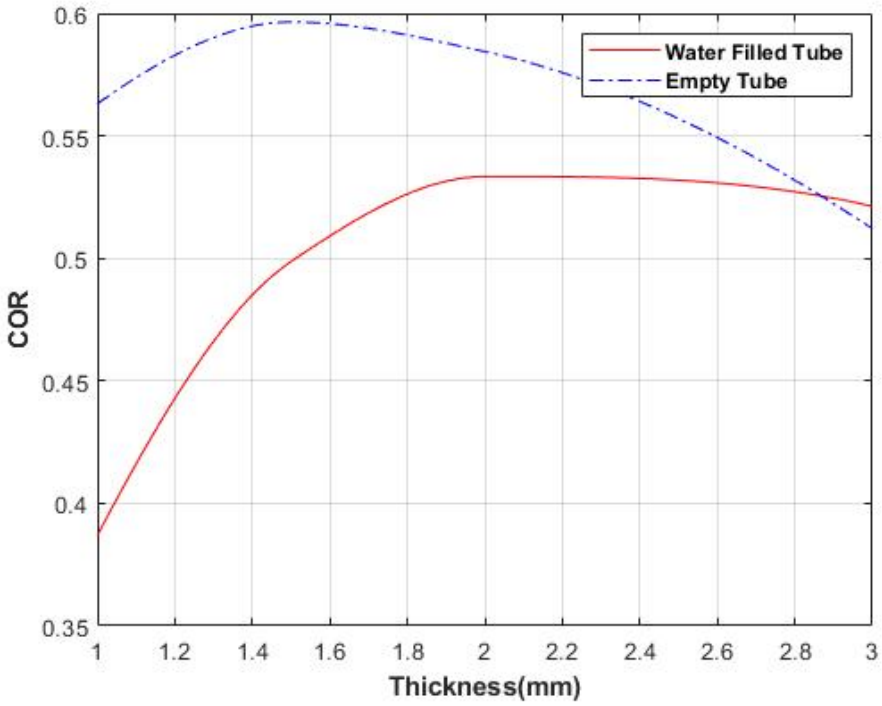

Figure 4.4: COR of a tube with the impact velocity of 3.8m/s

these criteria: 1) Penalty Formulation and 2) Lagrange Formulation. In penalty formulation, contact is treated as a stiff spring which resists penetration (ΔU) between bodies. This resistance is termed as contact stiffness, k, which is derived mainly as a function of material properties, geometries, and kinematics of the bodies. Two distinct contact stiffnesses are used for every contact analysis: one in the normal direction and the other in the tangential direction. In penalty formulation, two bodies can penetrate by small amounts during the interaction. This penetration is restored by contact formulation through opposing the penetration by a restoring force which is nothing but contact force, F. This contact force is a function of contact stiffness and the penetration as shown in Equation:4.1, below.

$$F = k\Delta U \tag{4.1}$$

In principle, the penalty formulation treats the contact as a stiff spring. The stiffness of this spring should be large enough to reduce the final penetration close to zero. The normal

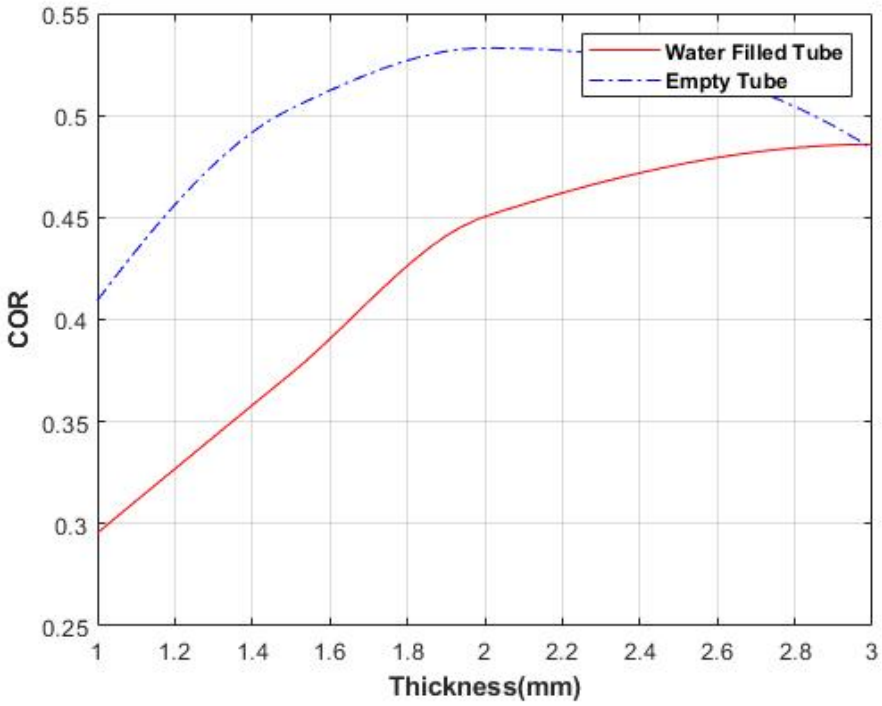

Figure 4.5: COR of a tube with the impact velocity of 6m/s

contact force is activated only when ΔU is negative, i.e.

$$F_n = \begin{cases} 0 & \text{for } \Delta U_n \geq 0 \\ k_n \Delta U_n & \text{for } \Delta U_n \leq 0 \end{cases} \tag{4.2}$$

In case of tangential contact forces τ, considering ΔU_1 and ΔU_2 as the lateral penetrations or slip distance and μ to be the coefficient of friction, the expression is given Equation 4.3below:

$$\tau_i = \begin{cases} k_t V_i & \text{if } ||\tau|| = \sqrt{{\tau_1}^2 + {\tau_2}^2} - \mu F_n \leq 0 \text{ (sticking)} \\ \mu F_n \dfrac{\Delta U_1}{||\Delta U_i||} & \text{if } ||\tau|| = \sqrt{{\tau_1}^2 + {\tau_2}^2} - \mu F_n = 0 \text{ (sliding)} \end{cases} \tag{4.3}$$

In Lagrange formulation, the contact is treated as a constraint, which means that this formulation enforces zero penetration throughout the simulation. Contact force is represented as contact traction vector F_R, and then the zero penetration boundary conditions are

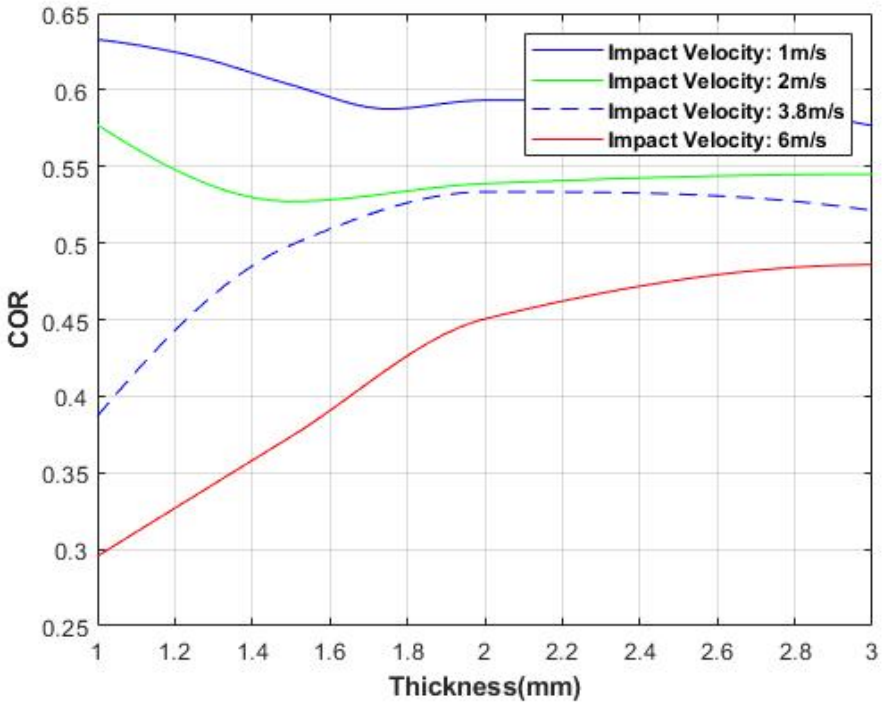

Figure 4.6: COR of a water-filled tube with the different impact velocities

applied at the interface of the bodies undergoing contact.

$$[F_R] = [F_n, V, \tau_1, \tau_2, \Delta U_1, \Delta U_2]^T \tag{4.4}$$

Adding these strong constraints at each node will make simulation by Lagrange formulation computationally very expensive. Until the penetration and hourglass energy is kept close to zero, the penalty method can be used to simulate the problems like low velocity impact of rods. Hence, all the contact force obtained by the simulation is based on penalty formulation. In order to validate the simulating results, the contact force of a solid rod is compared to analytical results (see Figure 4.8). The contact force results are in co-relation with the contact force solution obtained by the modified Jackson Green model of impact analysis.

Contact force on empty and fluid-filled tubes is tracked during the impact. Figures: 4.10 and 4.9 represent the base deformation versus the contact force of the water-filled and empty tubes with different thicknesses during the impact. This graph provides the data on

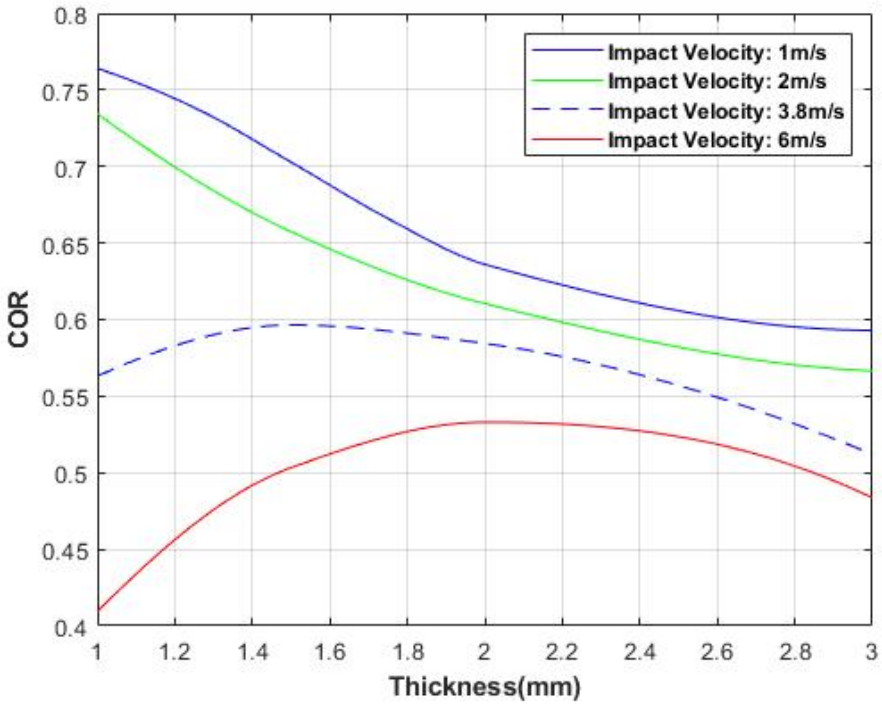

Figure 4.7: COR of an empty tube with the different impact velocities

the permanent deformation on the base after impact and the variation of contact force for different thicknesses of tubes. Showing contact force versus time, Figure 4.8 also provides information on the duration of the compression phase and the restitution phase. Analyzing the data provides insight on the effect of fluid during the impact of deformation and the impact duration. It is obvious that as tube thickness decreases, because of the fluid mass, the deformation of the base increases for the fluid filled tubes compared to empty tubes. However the amount of increase in permanent deformation of the base by the fluid-filled tubes is also depended on the impact velocity. As the impact velocity increases, the difference between the deformation of the base when the empty tubes and fluid-filled tubes impact tends to decrease. Considering both bodies undergoing the impact are subjected to deformation, for higher velocities, the tube tends to undergo more plastic deformation compared to the base it is impacting.

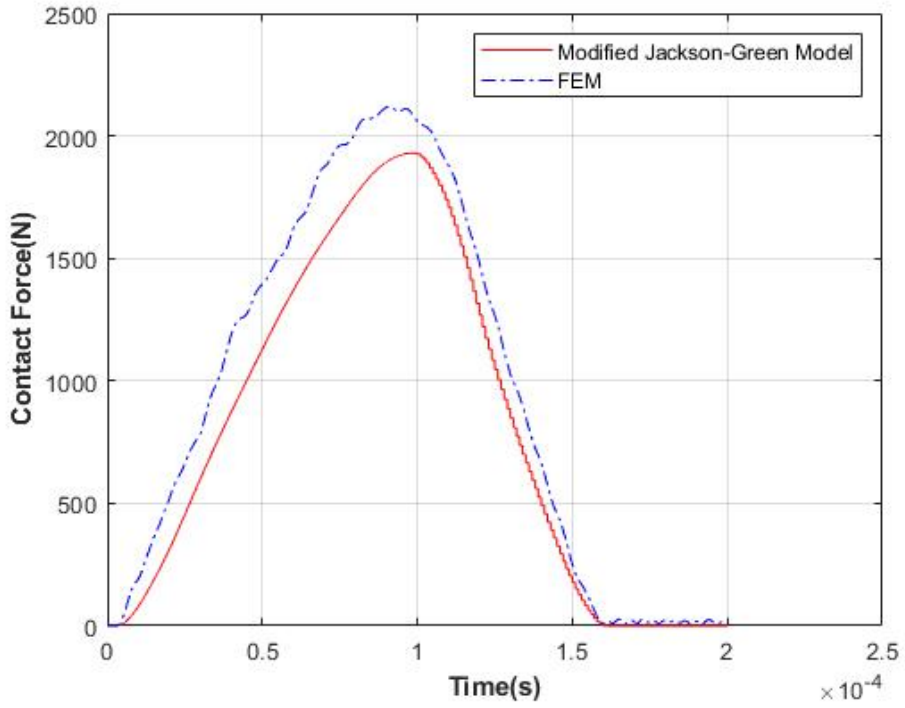

Figure 4.8: Contact force of rod of 5mm diameter impacting at 2m/s

4.4 The energy summary during the event of impact

An energy summary of a dynamic event is obtained for individual parts. An energy summary is also important to measure the accuracy of a simulation. The hourglass energy over the period of the simulation provides the deviation of simulated results from the energy balance equation. The hourglass energy is maintained to be zero for all the simulations done in this study. With making sure that there is no errors in the energy summary, the internal energy, kinetic energy and plastic work done by the parts during the event of impact is analyzed. Plastic work is a result of material plasticity that is an integral of the plastic strains over the duration of the impact(loading). It can be calculated as area under the stress, plastic strain curve as represented by Equation 4.5. Internal energy is the sum of plastic work and hourglass energy.

$$k = \int \sigma^T [M] d\epsilon^{pl} \tag{4.5}$$

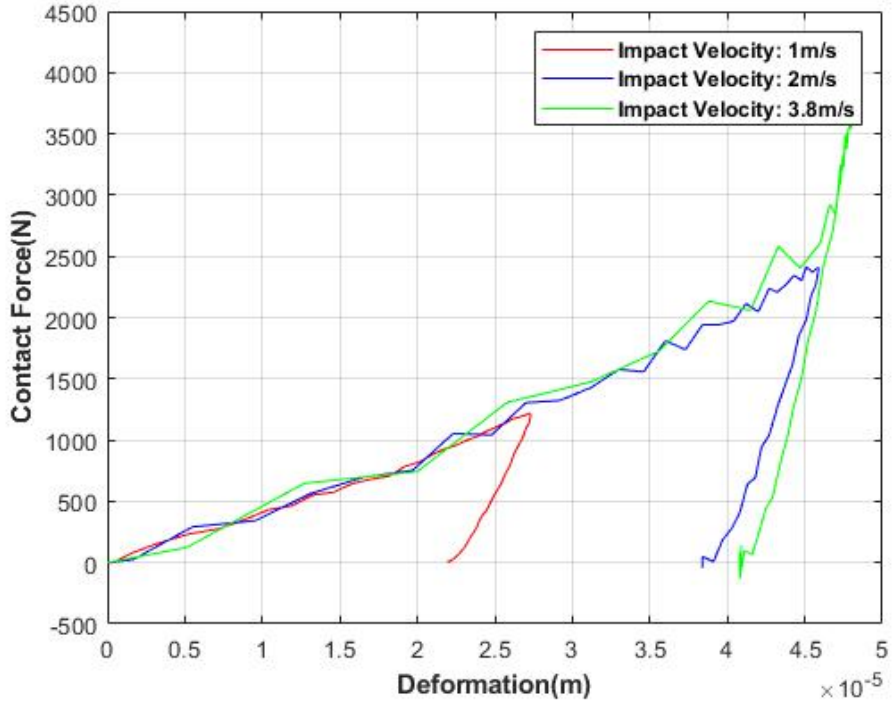

Figure 4.9: Contact force vs deformation of the base of a fluid-filled rod of 1mm thickness

Figure 4.11 represents the plastic work by a tube of 1mm thickness impacting from different drop heights. From this graph, it is obvious that the tube undergoes more plastic work when impacting from a greater drop height. Figure 4.12 shows the plastic behavior of the fluid filled tubes with different thicknesses impacting with different drop heights. This behavior is also consistent with different thicknesses and irrespective of if it is an empty tube or fluid-filled tube.

Figure:4.13 shows the difference between the plastic work done on the base by one of the empty and one of the fluid-filled tubes impacting at a velocity of 2 m/s. Similarly Figure:4.14 shows the difference between the plastic work done on the same tubes. Observing both graphs, we can infer that as the tube gets thinner the presence of fluid in the tube had no effect on the plastic work done on the base. All the energy of the impact is dissipated on the plastic deformation of tube rather than the base on which it is impacting. Additionally, plastic work done on the base is decreased for the impact of thinner tubes irrespective of the presence of fluid inside it (see Figure 4.15).

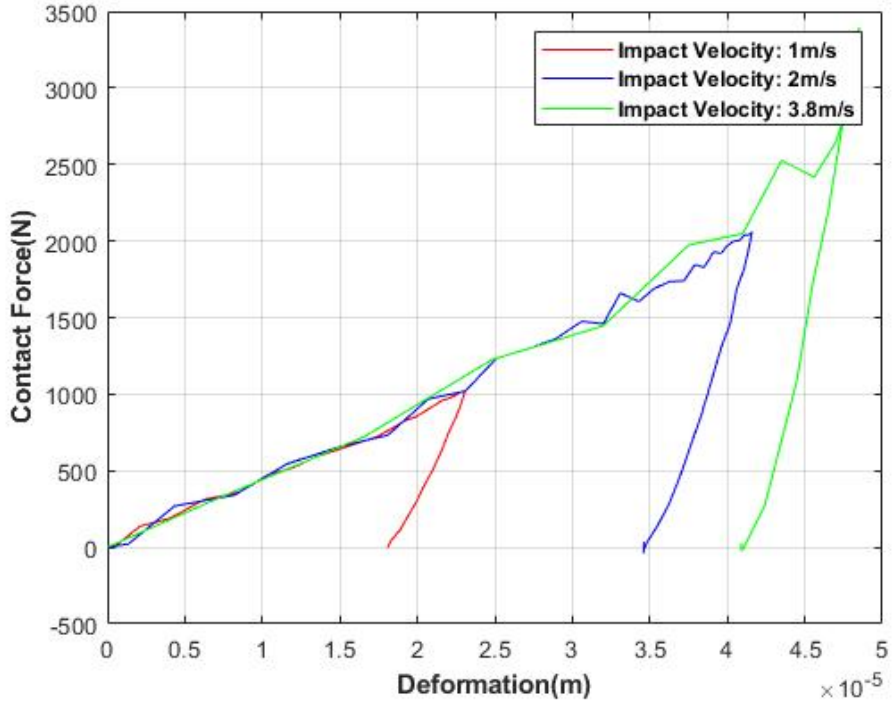

Figure 4.10: Contact force vs deformation of the base of an empty rod of 1mm thickness

4.5 Oblique impact of the fluid filled tubes

In this section, the oblique impact of the fluid-filled rod is simulated to measure the effect of fluid coupling on the impact parameters of the rod. Simulation is carried out using a Lagrangian reference frame. Tubes with diameters ranging from 10mm to 50mm, lengths ranging from 0.2m to 0.9m, and inclines of different angles are subjected to impact on a flat base. The simulation is carried out for different impact velocities and for both solid rods and tubes with different thicknesses. The rebound angular velocities are calculated using Equation 3.2.

During the restitution phase after the initial impact, it is observed that the tubes tend to have multiple impacts before rebounding completely. This behavior can be attributed to the bending modes of the tubes. At the point of impact, the tube is exited to vibrate in its first bending mode frequency. In this study, the significance of the bending modes of tube on the impact duration and resulting multiple impacts in the restitution phase is analyzed. If

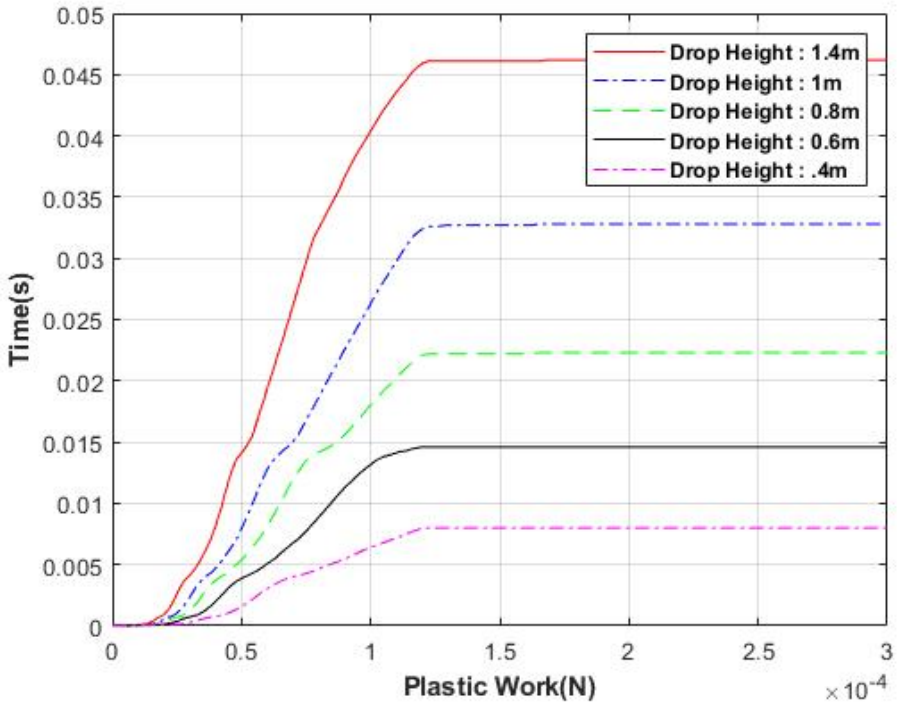

Figure 4.11: Plastic-Work on a fluid-filled tube impacting with different drop heights

the time duration of the bending mode is significantly more than the first impact duration, the tube tends to undergo a second impact on the base approximately within a half-wave duration of the bending mode. This can be observed in the impact of long slender rods [3][25][60][36].

Thus, total impact duration is significantly increased. As the natural bending mode frequency is significantly affected by the fluid coupling (see Chapter 2) so are the impact duration of the fluid-filled tubes and the time delay between multiple impacts. Figure 4.16 shows the relationship between the bending mode and the multiple impacts of the tube. If the modal frequency of the tube system is maintained relatively highly compared to the reciprocal of the initial impact duration, these multiple impacts can be avoided (see Table 4.1).

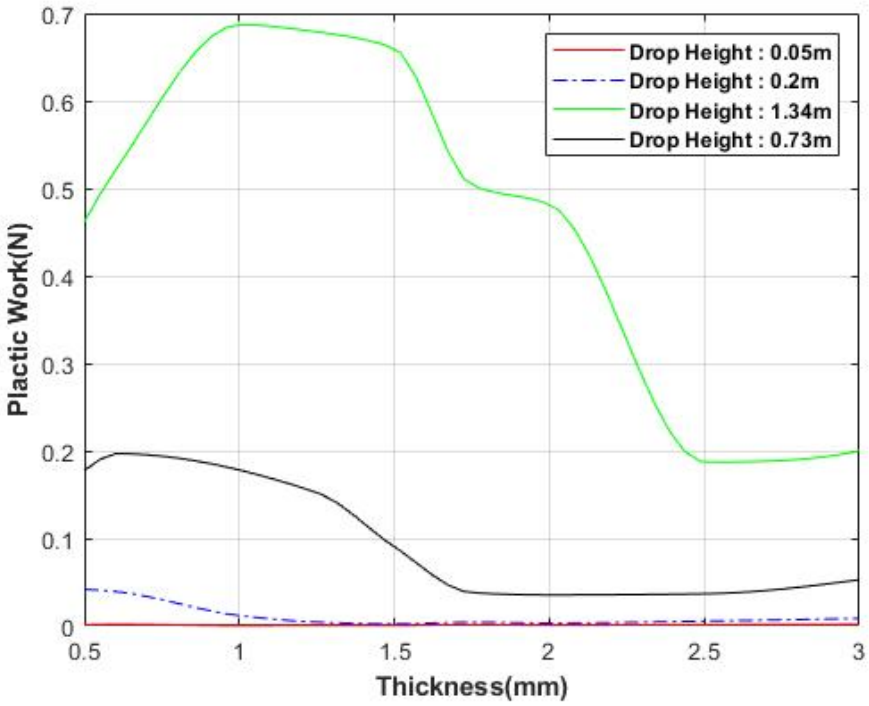

Figure 4.12: Plastic-Work on fluid-filled tubes with different thicknesses impacting with different drop heights

4.6 Conclusion

In this study, the effect of fluid structure interactions during impact is analyzed. The simulation results show that the COR of fluid-filled tubes decreases drastically when the thickness or the impact velocity is over a certain limit. This limit on the thickness of the tube matches the strong coupling condition proposed in Equation 2.22. The simulation of the contact force for a solid tube is validated by comparing the results with the modified Jackson Green model for the same rod. The contact force plots of fluid-filled tubes and empty tubes show that for a larger impact velocity, even though the contact force is increased in the presence of fluid, the deformation of the base is least affected by the presence of the fluid. Thus, for higher velocities, the tube tends to undergo more plastic deformation compared to the base it is impacting. There is a similar response with the energy summary of the impact. In the simulation of oblique impact of the rods and tubes, it was observed that the

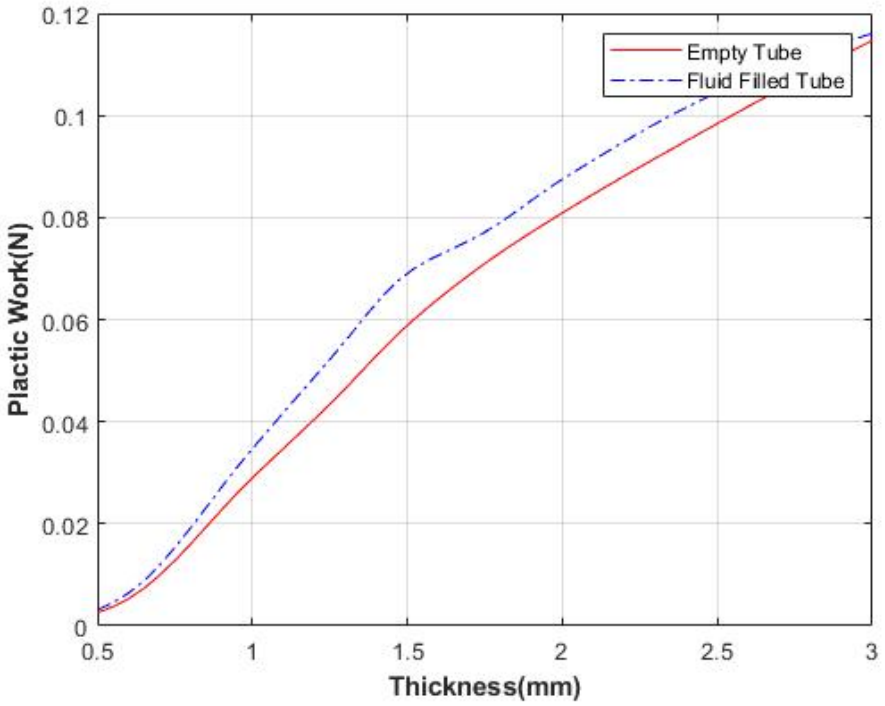

Figure 4.13: Difference in plastic-work on the base impacted by empty and fluid-filled tubes with different thicknesses

rod or tube undergoes multiple impacts during the restitution phase. This behavior can be linked to the bending mode of the natural frequency of the fluid-coupled tubes. It is also shown that if the natural bending frequency of the system is large enough compared to the reciprocal of the first impact duration, then there will be no multiple impacts of the rod.

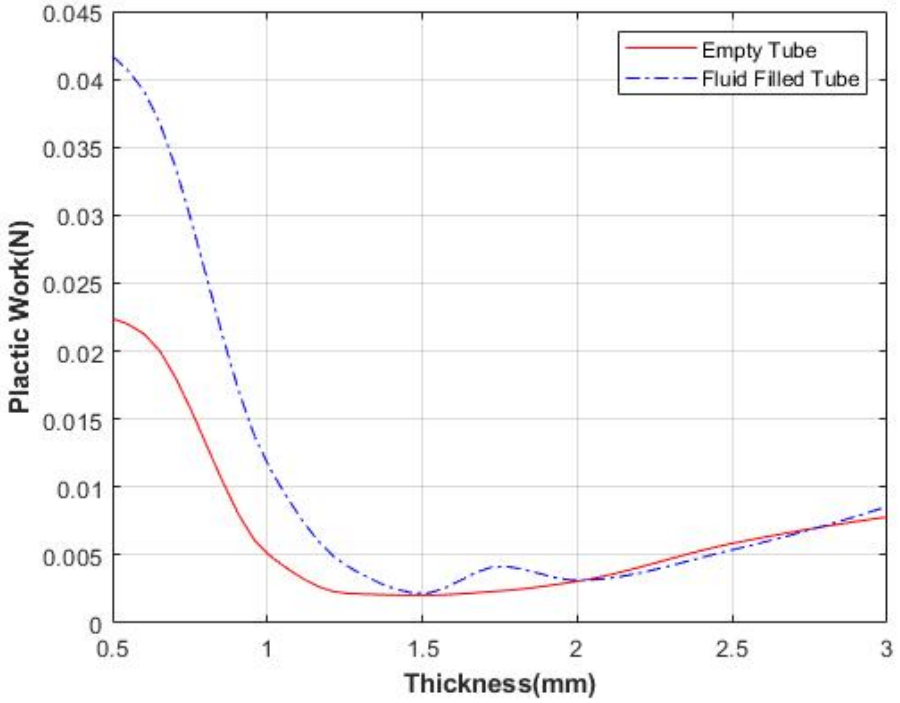

Figure 4.14: Difference in the plastic-work on the tube impacting with and without fluid

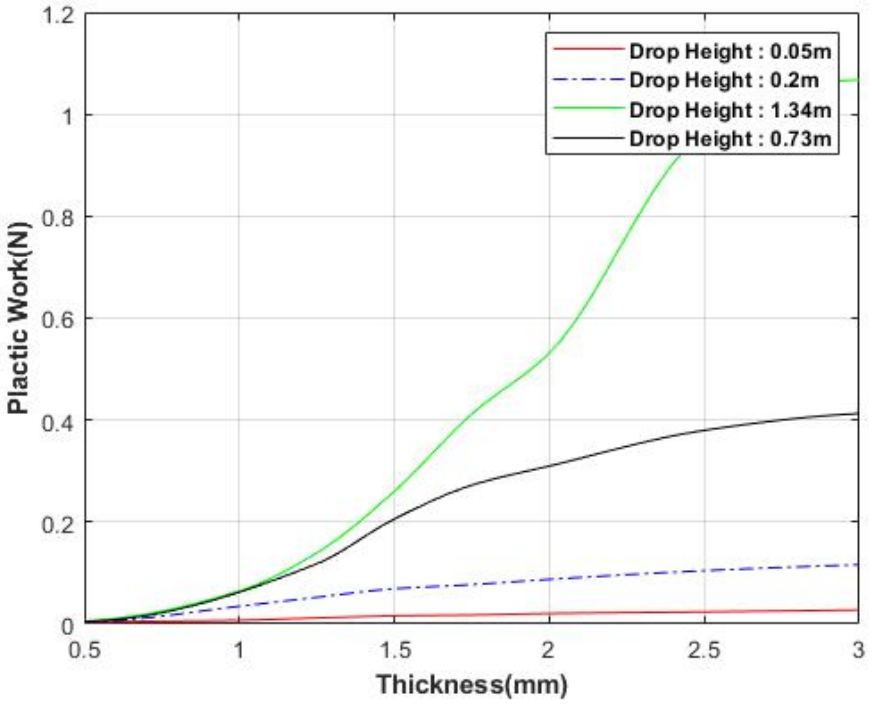

Figure 4.15: Plastic-work on the base by fluid-filled tubes impacting from different drop heights

Table 4.1: Relating the half-wave period to the impact duration and secondary impact of the rods and tubes

Bending Mode (Hz)	Half Wave Period (s) (1/2*Bending Mode)	First Impact Duration (s)	Time Diffrence Between Impacts (s)
450	1.111	1.002	1.212
604	0.828	0.630	0.871
665	0.752	0.619	0.884
1180	0.424	0.294	0.432
1180	0.424	0.306	0.444
1180	0.424	0.336	0.486
1300	0.385	0.270	0.421
1314	0.381	0.275	0.410
1347.5	0.371	0.259	0.394
1438	0.348	0.251	0.381
2179.9	0.229	0.366	
2470	0.202	0.438	

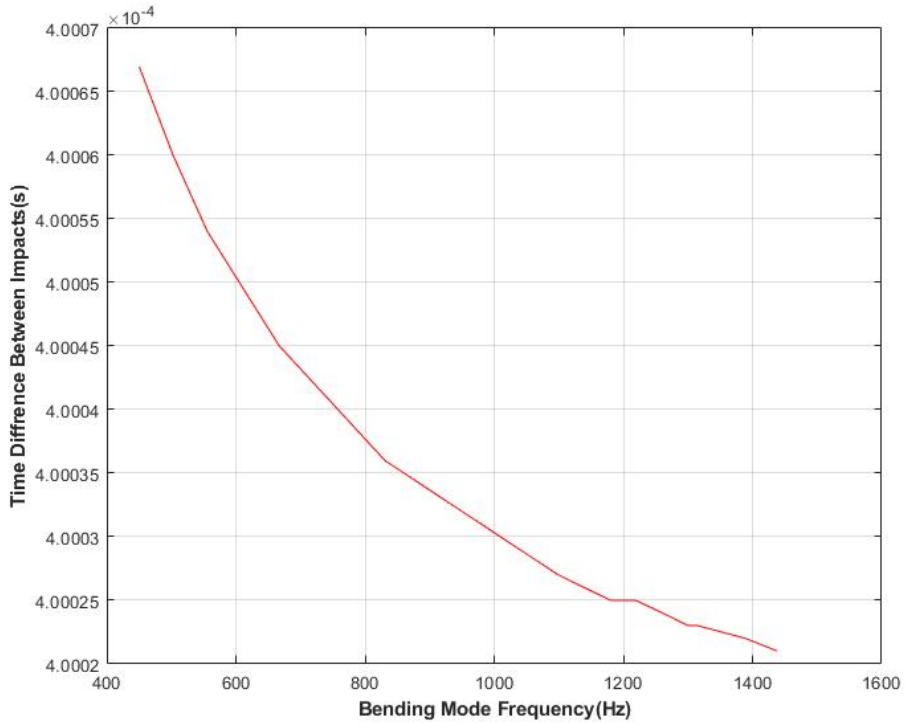

Figure 4.16: Correlation between the modal frequency and the secondary impact

Chapter 5

Conclusion and contribution

This research was an attempt to study the modal and impact interactions of fluid-filled cylindrical structures using the finite element methods. It is the first of its kind to describe the coupled natural frequency of the fluid-filled structure as a function of the respective modes of the uncoupled structures to differentiate strong and weak couplings. It is the first of its kind to simulate and validate the dynamic 3D event of the impact of a rod with a flat surface to analyze the impact behavior of the two bodies without any predefined assumptions with respect to boundary conditions or material properties.

Chapter 2 of the study is a parametric modal analysis of fluid-coupled thin structures. Here, the whole 3D geometry and modal simulation and 2-way fluid structure coupling are coded using ANSY APDL, which can be a resource for similar studies with different geometries. Junger's [27] approach to fluid-structure coupling is used to validate the modal simulation by our finite element analysis; consequently, this modeling and simulation technique is validated for modal analysis of fluid-structure coupling in any geometries. In the next step, parameters affecting the natural frequency of the cylinders have been examined in various combinations of geometries, materials and boundary conditions of thin walled structures and fluids. We proposed a termed called the *Coupling Factor* in Equation 4.1 for predicting the natural frequency of the coupled system for the given uncoupled natural frequency of the cylinder of the same mode. The importance of the coupling factor in the modal analysis of the fluid-coupled structures is shown through the study and realized by the proposed expression Equation 2.21. We proposed an apparent transition condition (see Equation 2.22) to differentiate strong and weak coupling of the cylinder structure with fluids. This study will serve as a guide for the further parametric FEM analysis on fluid-structure coupling

of similar systems and to gain insight into coupling factors. The presented conditions for the coupling factor and weak and strong coupling will serve as a guide for the design of cylindrical structures.

In Chapter 3, the objective was to find an optimized method to simulate the dynamic 3D event of the impact of a rod with a flat surface. To the best of our knowledge, all the contact models are quasi-static with predefined 2D symmetric contacts, whereas this study focuses on modeling and simulating the dynamic 3D event of the impact with no predefined analytical constraints. The beginning of this study review the prominent contact and plasticity models of contact analysis in FEM. In the next step, experiments of the impact of rods on a flat base were conducted with the help of a high-speed camera. Both normal and oblique impacts of all the rods were recorded. These visuals were used to track the rod during and after the event of impact. The rebound velocity and angular velocity, and thus the coefficient of restitution(COR), of different rods were tabulated. Experimental results of permanent deformation on the base for different impact velocities were derived out of a prominent impact study. These systems were modeled in an 'ANSYS Workbench Explicit Dynamics' module for the simulation. Different plasticity models were studied and analyzed to apply appropriate material properties for the rods and base. For the simulation of low velocity impacts, this study will offer guidance to choosing proper plasticity models for materials based on their requirements. After running the simulation, the COR were compared with the experimental results for both normal and oblique impact. These simulation results correlated well with the experimental results, thus validating the simulation method used for analysis of low-velocity impact. Furthermore, other impact parameters like deformations and contact force were correlated with different prominent contact models. To further validate the dynamic behavior, stress waves in the tube after impact were calculated through simulation to match the sound velocity in the material of the rod. With these comparisons, it can be inferred that the 3D explicit dynamics analysis presented in this study is valid

for low-velocity impact analysis. Unlike the 2D FEM based predefined contact models, this validated 3D explicit dynamic simulation provides more information on the impact behavior than the just contact force and deformation. The coefficient of restitution, vibration, plastic work, energy summary of the system, and other dynamic behaviors can be and are studied. The presented modeling and simulation technique can serve as a guide in the designing of robotic arms, where these low-velocity impacts are more prevalent. Given that there are no predefined conditions in the proposed simulation method of impact, this technique can be used to simulate and study the low-velocity impact behavior of composite structures.

Finally in Chapter 4, the focus was on analyzing the effect of fluid-structure interactions during impact. Two different techniques are proposed to model the water filled tubes impacting a flat base. A Lagrangian reference frame is used to model the fluid elements instead of a Eulerian reference frame, as Lagrangian reference frame is more efficient in terms of computational time and accurate enough for the analysis of low-velocity impacts. The COR of the water-filled tubes provided insight into how the fluid-filled tube behaves during the event of impact. Further in the study, a brief explanation is provided on principles used in FEM to detect and formulate the contacts between two bodies like in an impact. Contact force and energy on the empty and fluid-filled tubes are tracked during the impact. A probable explanation for variation and the effect of fluids and impact velocities on the contact force and deformation is proposed. Finally, in the simulation of oblique impact of the rods and tubes, it was observed that the rod or tube undergoes multiple impacts. In this study, it is proposed that the bending mode of the natural frequency is the reason for this behavior of multiple impacts, thought this needs to be validated by experiments in further studies.
This research includes the following publications:
- "Modal analysis of coupled structures and parametric relation of the coupled and uncoupled natural frequency of cylinders by finite element analysis" in the International Journal of Engineering Applied Science and Technology (IJEAST).

- "Simulation of dynamic event of impact using explicit 3D FEM model and validation by experiment and contact models" in the International Journal of Engineering Applied Science and Technology (IJEAST).
- "Effect of modal frequency in the oblique impacts of fluid coupled cylinders" under review.

Bibliography

[1] High velocity impact of segmented rods with an aluminum carrier tube. *International Journal of Impact Engineering*, 17(4):915–923, 1995.

[2] Finite element simulation of microindentation on aluminum. *Journal of Materials Science*, 36(8):1943–1949, Apr 2001.

[3] The break-up tendency of long rod projectiles. *Defence Technology*, 12(2):177–187, 2016.

[4] J. Alcalá and D. Esqué-de los Ojos. Reassessing spherical indentation: Contact regimes and mechanical property extractions. *International Journal of Solids and Structures*, 47(20):2714 – 2732, 2010.

[5] M. Amabili, F. Pellicano, and M.P. Paidoussis. Nonlinear vibrations of simply supported, circular cylindrical shells, coupled to quiescent fluid. *Journal of Fluids and Structures*, 12(7):883 – 918, 1998.

[6] Marco Anghileri, Luigi-M.L. Castelletti, and Maurizio Tirelli. Fluid–structure interaction of water filled tanks during the impact with the ground. *International Journal of Impact Engineering*, 31(3):235–254, 2005.

[7] A.G. Atkins and D. Tabor. Plastic indentation in metals with cones. *Journal of the Mechanics and Physics of Solids*, 13(3):149 – 164, 1965.

[8] S.Subhash Babu and S.K. Bhattacharyya. Finite element analysis of fluid-structure interaction effect on liquid retaining structures due to sloshing. *Computers Structures*, 59(6):1165–1171, 1996.

[9] Klaus-Jurgen Bathe. *Finite Element Procedures*. Prentice Hall, 1996.

[10] Eren Billur and Muammer Koç. Formability of austenitic stainless steels under warm hydroforming conditions. *Transactions of the North American Manufacturing Research Institution of SME*, 37:1, 01 2009.

[11] M.R.W. Brake. An analytical elastic plastic contact model with strain hardening and frictional effects for normal and oblique impacts. *International Journal of Solids and Structures*, 62:104 – 123, 2015.

[12] D H Chambers. *Acoustically Driven Vibrations in Cylindrical Structures*. Lawrence Livermore National Lab. (LLNL), Livermore, 2013.

[13] Peter Davidsson. *Structure-acoustic analysis; finite element modelling and reduction methods*. PhD thesis, Lund University, 2004.

[14] T. De Vuyst, R. Vignjevic, and J.C. Campbell. Coupling between meshless and finite element methods. *International Journal of Impact Engineering*, 31(8):1054–1064, 2005.

[15] Giovanni Ferrari, Prabakaran Balasubramanian, Stanislas Le Guisquet, Lorenzo Piccagli, Kostas Karazis, Brian Painter, and Marco Amabili. Non-linear vibrations of nuclear fuel rods. *Nuclear Engineering and Design*, 338:269–283, 2018.

[16] A. C. Fischer-Cripps. Elastic–plastic behaviour in materials loaded with a spherical indenter. *Journal of Materials Science*, 32(3):727–736, Feb 1997.

[17] Hamid Ghaednia, Dan B. Marghitu, and Robert Jackson. Predicting the permanent deformation after the impact of a rod with a flat surface. *Journal of Tribology*, 137:011403, 10 2014.

[18] Hamid Ghaednia, Gregory Mifflin, Priyansh Lunia, Eoghan O. O'Neill, and Matthew R. W. Brake. Strain hardening from elastic-perfectly plastic to perfectly elastic indentation single asperity contact. *Frontiers in Mechanical Engineering*, 6:60, 2020.

[19] Hamid Ghaednia, Xianzhang Wang, Swarna Saha, Yang Xu, Aman Sharma, and Robert Jackson. A review of elastic-plastic contact mechanics. *Applied Mechanics Reviews*, 69, 04 2018.

[20] C. Hardy, C. N. Baronet, and G. V. Tordion. The elasto-plastic indentation of a half-space by a rigid sphere. *International Journal for Numerical Methods in Engineering*, 3:451–462, 1971.

[21] Shao Hsia and Yu-Tuan Chou. Fabrication improvement of cold forging hexagonal nuts by computational analysis and experiment verification. *Mathematical Problems in Engineering*, 2015:835038, 12 2015.

[22] Shao Hsia and Yu-Tuan Chou. An investigation of the elastic cylindrical line contact equations for plane strain and stress considering friction. *Journal of Engineering Tribology*, 2019:835038, 1 2021.

[23] Robert Jackson, Itti Chusoipin, and Itzhak Green. A Finite Element Study of the residual stress and deformation in hemispherical contacts. *Journal of Tribology*, 127:484, 07 2005.

[24] K. L. Johnson. The correlation of indentation experiments. *Journal of Mechanics Physics of Solids*, 18:115–126, April 1970.

[25] W. Johnson, S.R. Reid, A.K. Sengupta, and S.K. Ghosh. Modelling with plasticine the low speed impact of long rods against inclined rigid targets. *International Journal of Impact Engineering*, 1(1):73–83, 1983.

[26] Norman Jones and R.S. Birch. Low-velocity impact of pressurised pipelines. *International Journal of Impact Engineering*, 37(2):207–219, 2010.

[27] M.C. Junger and D. Feit. *Sound, Structures, and Their Interaction*. MIT Press, 1972.

[28] F. Katsamanis and W. Goldsmith. Transverse Impact on Fluid-Filled Cylindrical Tubes. *Journal of Applied Mechanics*, 49(1):149–156, 03 1982.

[29] Etsion I. Kogut, L. Elastic-plastic contact analysis of a sphere and a rigid flat. *Journal of Applied Mechanics*, 69:657–662, 8 2002.

[30] L. Kogut and K. Komvopoulos. Analysis of the spherical indentation cycle for elastic–perfectly plastic solids. *Journal of Materials Research*, 19(12):3641–3653, 2004.

[31] K. Komvopoulos and N. Ye. Three-dimensional contact analysis of elastic-plastic layered media with fractal surface topographies. *Journal of Tribology-transactions of The Asme*, 123:632–640, 07 2001.

[32] Komvopoulos K. Bogy D. B. Kral, E. R. Elastic-plastic finite element analysis of repeated indentation of a half-space by a rigid sphere. *Journal of Applied Mechanics*, 60:829–841, 1993.

[33] Ram Kumar. Flexural vibrations of fluid-filled circular cylindrical shells. *Acustica*, 24(3):137–146, 1971.

[34] C.S.W. Lavooij and A.S. Tusseling. Fluid-structure interaction in liquid-filled piping systems. *Journal of Fluids and Structures*, 5(5):573–595, 1991.

[35] Q. S. Li, Ke Yang, and Lixiang Zhang. Analytical solution for fluid-structure interaction in liquid-filled pipes subjected to impact-induced water hammer. *Journal of Engineering Mechanics*, 129(12):1408–1417, 2003.

[36] E. Lidén, B. Johansson, and B. Lundberg. Effect of thin oblique moving plates on long rod projectiles: A reverse impact study. *International Journal of Impact Engineering*, 32(10):1696–1720, 2006.

[37] G.Y. Lu, Z.J. Han, J.P. Lei, and S.Y. Zhang. A study on the impact response of liquid-filled cylindrical shells. *Thin-Walled Structures*, 47(12):1557–1566, 2009.

[38] Damodar Maity and Sriman Kumar Bhattacharyya. A parametric study on fluid–structure interaction problems. *Journal of Sound and Vibration*, 263, 2003.

[39] Akshay Mallikarjuna, Dan Marghitu, and P.K.Raju. Simulation of dynamic event of impact using explicit 3D FEM model and validation by experiment and contact models. *International Journal of Engineering Applied Sciences and Technology*, 6(3):51–61, 2021.

[40] Akshay Mallikarjuna, Dejiang Shang, and P.K.Raju. Modal analysis of coupled structures and parametric relation of the coupled and uncoupled natural frequency of cylinders by finite element analysis. *International Journal of Engineering Applied Sciences and Technology*, 4(4):323–335, 2019.

[41] Sinisa Mesarovic and Norman Fleck. Spherical indentation of elastic–plastic solids. *Proceedings of The Royal Society A Mathematical Physical and Engineering Sciences*, 455:2707–2728, 07 1999.

[42] Siva Naga Venkata Ravi Kiran Kurapati. *Elastic-Plastic Indentation Deformation in Homogeneous and Layered Materials: Finite Element Aanalysis*. PhD thesis, University of Kentucky, 03 2019.

[43] N Ogbonna, Norman Fleck, and Alan Cocks. Transient creep analysis of ball indentation. *International Journal of Mechanical Sciences*, 37:1179–1202, 11 1995.

[44] Niels Saabye Ottosen. *Introduction to the Finite Element Method*. Prentice Hall, 1992.

[45] Raymond Panneton and Noureddine Atalla. Numerical prediction of sound transmission through finite multilayer systems with poroelastic materials. *The Journal of the Acoustical Society of America*, 100(346), 1996.

[46] Luigi Perotti, Ralf Deiterding, Kazuaki Inaba, Joseph Shepherd, and Michael Ortiz. Elastic response of water-filled fiber composite tubes under shock wave loading. *International Journal of Solids and Structures*, 50:473–486, 02 2013.

[47] P.E. Reed, G. Breedveld, and B.C. Lim. Simulation of the drop impact test for moulded thermoplastic containers - precursor waves and mechanical damping. *International Journal of Impact Engineering*, 24:133–153, 02 2000.

[48] A. Renger. Johnson, k. l., contact mechanics. cambridge etc., cambridge university press 1985. xii, 452 pp., £ 17.50 p/b. isbn 0521347963. *ZAMM - Journal of Applied Mathematics and Mechanics / Zeitschrift für Angewandte Mathematik und Mechanik*, 69(7):214–214, 1989.

[49] ANSYS $AcademicResearch. AcousticFluid - StructuralInteraction(FSI) - 8.4. ANSYS, Inc.$

[50] ANSYS $AcademicResearch. Acoustic\ Fundamentals\ -\ 8.1. ANSYS, Inc.$

[51] ANSYS $AcademicResearch. CoupledEffects - 10.1. ANSYS, Inc.$

[52] ANSYS $AcademicResearch. Eigenvalue\ and\ Eigenvector\ Extraction\ -\ 14.14. ANSYS, Inc.$

[53] ANSYS $AcademicResearch. Mode\ -\ Frequency\ Analysis\ -\ 15.3. ANSYS, Inc.$

[54] Anthony Sanders, Ira Tibbitts, Deepika Kakarla, Stephanie Siskey, Jorge Ochoa, Kevin Ong, and Rebecca Brannon. Contact mechanics of impacting slender rods: Measurement and analysis. *Conference Proceedings of the Society for Experimental Mechanics Series*, 1:229–236, 05 2011.

[55] W. J. Stronge. Energy dissipated in planar collision. *Journal of Applied Mechanics*, 63:681–682, 1992.

[56] W. J. Stronge and William Johnson. Rigid body collisions with friction. *Proceedings of the Royal Society of London. Series A: Mathematical and Physical Sciences*, 431(1881):169–181, 1990.

[57] Arris Tijsseling, Martin Lambert, Angus Simpson, Mark Stephens, John Vítkovský, and Anton Bergant. Skalak's extended theory of water hammer. *Journal of Sound and Vibration*, 310:718–728, 01 2008.

[58] J. S. Walker and J. W. Phillips. Pulse Propagation in Fluid-Filled Tubes. *Journal of Applied Mechanics*, 44(1):31–35, 03 1977.

[59] G. B. Warburton. Vibration of a cylindrical shell in an acoustic medium. *Journal of Mechanical Engineering Science*, 3(1):69–79, 1961.

[60] Xin-Ke Xiao, Zi-Tao Guo, Zhong-Cheng Mu, and Wei Zhang. Preliminary Study on Water Filled Tank Perforation by Rod Projectiles. In *APS Shock Compression of Condensed Matter Meeting Abstracts*, APS Meeting Abstracts, 2009.

[61] Huaidong Yang and Itzhak Green. Fretting Wear Modeling of Cylindrical Line Contact in Plane-Strain Borne by the Finite Element Method. *Journal of Applied Mechanics*, 86(6), 04 2019. 061012.

[62] Zeng Qingliang Yang, Yang. Contact response analysis of vertical impact between elastic sphere and elastic half space. *Journal of Shock and Vibration*, 2018:1802174, 2018.

[63] Zhang Zhiqiang Yang Jialing Sun Yuxin Yang, Xianfeng. Fluid–structure interaction analysis of the drop impact test for helicopter fuel tank. *SpringerPlus*, 5:1573, 2016.

[64] Komvopoulos K. Ye, N. Indentation analysis of elastic-plastic homogeneous and layered media: Criteria for determining the real material hardness. *Journal of Tribology*, 185:685–691, 2003.

[65] Jeong Ho You and K. Inaba. Fluid–structure interaction in water-filled thin pipes of anisotropic composite materials. *Journal of Fluids and Structures*, 36:162–173, 2013.

[66] Cao Yuan and Jin Xianlong. Dynamic response of flexible container during the impact with the ground. *International Journal of Impact Engineering*, 37(10):999–1007, 2010.

[67] Ainian Zhang and Katsuyuki Suzuki. A comparative study of numerical simulations for fluid–structure interaction of liquid-filled tank during ship collision. *Ocean Engineering*, 34:645–652, 04 2007.

[68] Guo J. Guo J.Y. Guo R. Zhang Y.T., Zhang W.M. Analysis on the effects of the shapes of flexible fluid-filled containers on their impact response. *International Journal of Heat and Technology*, 35:139–146, 2017.